Published for SISSA by Springer

Received: *January 17, 2017*
Revised: *October 30, 2017*
Accepted: *November 23, 2017*
Published: *December 1, 2017*

The decay constants f_D and f_{D_s} in the continuum limit of $N_f = 2+1$ domain wall lattice QCD

The RBC/UKQCD collaboration

P.A. Boyle,[a] **L. Del Debbio,**[a] **A. Jüttner,**[b] **A. Khamseh,**[a] **F. Sanfilippo**[b] **and J.T. Tsang**[a,b]

[a] *Higgs Centre for Theoretical Physics, School of Physics & Astronomy,*
University of Edinburgh, EH9 3FD, U.K.
[b] *School of Physics and Astronomy, University of Southampton,*
Southampton, SO17 1BJ, U.K.

E-mail: `paboyle@ph.ed.ac.uk`, `luigi.del.debbio@ed.ac.uk`,
`a.juettner@soton.ac.uk`, `a.khamseh@sms.ed.ac.uk`,
`fr.sanfilippo@gmail.com`, `j.t.tsang@ed.ac.uk`

Abstract: We present results for the decay constants of the D and D_s mesons computed in lattice QCD with $N_f = 2+1$ dynamical flavours. The simulations are based on RBC/UKQCD's domain wall ensembles with both physical and unphysical light-quark masses and lattice spacings in the range 0.11–0.07 fm. We employ the domain wall discretisation for all valence quarks.

The results in the continuum limit are $f_D = 208.7(2.8)_{\rm stat}\left(^{+2.1}_{-1.8}\right)_{\rm sys}$ MeV and $f_{D_s} = 246.4(1.3)_{\rm stat}\left(^{+1.3}_{-1.9}\right)_{\rm sys}$ MeV and $f_{D_s}/f_D = 1.1667(77)_{\rm stat}\left(^{+57}_{-43}\right)_{\rm sys}$. Using these results in a Standard Model analysis we compute the predictions $|V_{cd}| = 0.2185(50)_{\rm exp}\left(^{+35}_{-37}\right)_{\rm lat}$ and $|V_{cs}| = 1.011(16)_{\rm exp}\left(^{+4}_{-9}\right)_{\rm lat}$ for the CKM matrix elements.

Keywords: Heavy Quark Physics, Lattice QCD, Lattice Quantum Field Theory, Quark Masses and SM Parameters

ArXiv ePrint: 1701.02644

https://doi.org/10.1007/JHEP12(2017)008

Contents

1 Introduction

The charmed D and D_s mesons decay weakly into a lepton and a neutrino. The experimental measurement of the corresponding decay rates together with their prediction from within the Standard Model (SM) provides for a direct determination of the CKM matrix elements $|V_{cd}|$ and $|V_{cs}|$. Leptonic $D_{(s)}$ decays have therefore been studied extensively by a number of experiments (CLEO-c [1–7], BES [8], Belle [9] and BaBar [10]). Together with the perturbative prediction of electroweak contributions in the SM this leads to the results [11]

$$|V_{cd}|f_{D^+} = 45.91(1.05)\mathrm{MeV}\,, \qquad |V_{cs}|f_{D_s^+} = 250.9(4)\mathrm{MeV}\,. \tag{1.1}$$

The reliable SM prediction for the decay constants

$$f_{D_q} = \frac{\langle 0|\, \bar{c}\gamma_0\gamma_5 q \,|D_q(0)\rangle}{m_{D_q}}, \qquad \text{where } q = d, s\,, \tag{1.2}$$

hence allows for the determination of $|V_{cd}|$ and $|V_{cs}|$ respectively. Combined with calculations of other CKM matrix elements [11, 12], a number of SM tests of, for instance, the unitarity of the CKM matrix can be devised (see e.g. refs. [13, 14]).

Surprisingly, relatively few state-of-the-art predictions for the decay constants with a reliable control of systematic uncertainties exist to date (see e.g. the discussion of the results of $N_f = 2{+}1$ [15–18] and $N_f = 2{+}1{+}1$ [19, 20] in the 2016 FLAG report [21]). The computation of decay constants in lattice QCD is by now a well established exercise and many results with sub-percent precision within isospin symmetric QCD do exist for pions and kaons. This is less so however in the case of the D- and D_s-meson decay constants. The major difficulty there lies in the fact that with the charm-quark mass slightly above 1 GeV, cut-off effects arising from the charm mass remain a serious concern in lattice simulations. Ensembles with dynamical quarks and sufficiently small lattice spacing to allow controlled continuum extrapolations have only become feasible in recent years.

Existing calculations try to deal with this in various ways by using discretisations tailored to reduce cut-off effects. For instance, highly improved staggered quarks [22], the Fermilab approach [23], overlap fermions [24], Osterwalder-Seiler fermions [19, 25] or non-perturbatively improved Wilson fermions [26, 27] are used as the charm-quark discretisation.

Here we present the first calculation of the D- and D_s-meson decay constants using the domain wall discretisation for the charm as well as the light and strange quarks on RBC/UKQCD's gauge ensembles with large volumes and physical values of the light-quark masses. Domain wall fermions (DWF) on the lattice provide chiral symmetry to a good approximation and, as a result of this, automatic $O(a)$ improvement. In particular, the leading discretisation effects are $O(a^2)$ and all odd powers of the lattice spacing are constrained to be absent by the chiral symmetry. This automatic improvement is important when discretising charm quarks since no further work is required for tuning improvement coefficients in the action and for operators.

Discretising both the light as well as the charm quark within the same framework allows to correctly reproduce GIM cancellation [28] in lattice computations. The suitability of domain wall charm quarks for SM phenomenology demonstrated in this work is an important ingredient for an entirely new class of lattice computations as for instance ϵ_K [29], ΔM_K [30] and processes such as $K \to \pi l^+ l^-$ [31, 32] and $K \to \pi\nu\bar{\nu}$ [33] which the RBC and UKQCD collaborations are pursuing.

Given the novel nature of domain wall fermions as heavy quark discretisation we have investigated their properties in detail in two preparatory publications [34, 35]. We studied the continuum limit behaviour of heavy-strange decay constants over a wide range of lattice cut-offs (2-6 GeV) within quenched QCD. In this way we determined parameters of the domain wall discretisation which resulted in small discretisation effects for charmed meson decay constants. Refs. [34, 35] show that DWF with suitably chosen parameters show mild cut-off dependence for charmed meson masses and decay constants. We expect this to hold also in the presence of sea-quarks on RBC/UKQCD's gauge ensembles, thus the study at hand.

This work summarises our computation within this setup of the D- and D_s-meson decay constants f_D and f_{D_s}, respectively, their ratio and the Cabibbo-Kobayashi-Maskawa (CKM) matrix elements $|V_{cd}|$ and $|V_{cs}|$. Note that all quoted results for the decay constants are for isospin symmetric QCD.[1] Systematic errors are due to choices made when fitting and parameterising the lattice data, lattice scale setting, finite volume, isospin breaking and renormalisation, based on $N_f = 2 + 1$ flavour simulations. Isospin breaking effects in the determination of CKM matrix elements are based on estimates. In the determination of the CKM matrix element the lattice statistical and systematic errors have been combined in quadrature.

The paper is structured as follows: in section 2 we summarise our numerical set up and give details of all simulation parameters. Section 3 presents our complete analysis for the $D_{(s)}$-meson decay constants and constitutes the main body of this paper. In section 4 we extract the corresponding CKM matrix elements before concluding in 5.

2 Numerical simulations

This report centres mainly around ensembles with physical light-quark masses in large volumes [37]. The data analysis will however also take advantage of information obtained on ensembles with unphysically heavy pions [38–40]. The gauge field ensembles we use (cf. table 1) represent isospin symmetric QCD with $N_f = 2 + 1$ dynamical flavours at three different lattice spacings in the range 0.11 fm-0.07 fm (**C**oarse, **M**edium and **F**ine). All ensembles have been generated with the Iwasaki gauge action [41, 42]. For the discretisation of the quark fields we adopt either the DWF action with the Möbius kernel [43–45] or the Shamir kernel [46, 47]. The difference between both kernels in our implementation corresponds to a rescaling such that Möbius domain wall fermions (MDWF) are numerically close to Shamir domain wall fermions (SDWF) at twice the extension in the fifth dimension [37]. Möbius domain wall fermions are hence cheaper to simulate while providing the same level of lattice chiral symmetry. Results from both formulations of domain wall fermions lie on the same scaling trajectory towards the continuum limit with cut-off effects starting at $O(a^2)$. Even these $O(a^2)$ cut-off effects themselves are expected to agree between our Möbius and Shamir formulations, with their relative difference at or below the level of 1% [37] for the finite values of the extent of the fifth dimension (L_s) used in our simulations.

Basic properties of all ensembles used in this work are summarised in tables 1 and 2. The lattice scale and physical light-quark masses have been determined for all ensembles bar F1 in [37] using m_π, the m_K and the m_Ω as experimental input. The finest ensemble F1 was generated later as part of RBC-UKQCD's charm and bottom physics program and its properties are described in appendix A. We repeated the analysis of [37] after including

---

[1] See [36] for a strategy to directly compute isospin breaking effects in meson decays.

Name	DWF	L/a	T/a	a^{-1}[GeV]	m_π[MeV]	hits/conf	confs	total
C0	MDWF	48	96	1.7295(38)	139.15(36)	48	88	4224
C1	SDWF	24	64	1.7848(50)	339.789(12)	32	100	3200
C2	SDWF	24	64	1.7848(50)	430.648(14)	32	101	3232
M0	MDWF	64	128	2.3586(70)	139.35(46)	32	80	2560
M1	SDWF	32	64	2.3833(86)	303.248(14)	32	83	2656
M2	SDWF	32	64	2.3833(86)	360.281(16)	16	77	1232
F1	MDWF	48	96	2.774(10)	234.297(10)	48	82	3936

Table 1. This table summarises the main parameters of our $N_f = 2 + 1$ ensembles. C stands for coarse, M for medium and F for fine, MDWF for Möbius and SDWF for Shamir DWF. The columns "hits/conf" and "confs" give the number of measurements on a given configuration and the total number of configurations used, respectively. The column "total" gives their product which is the total number of measurements carried out.

Name	DWF	M_5	L_s	am_l^{uni}	am_s^{uni}	am_s^{sim}	am_s^{phys}	$\Delta m_s/m_s^{\mathrm{phys}}$
C0	MDWF	1.8	24	0.00078	0.0362	0.0362	0.03580(16)	0.0112(45)
C1	SDWF	1.8	16	0.005	0.04	0.03224, 0.04	0.03224(18)	—
C2	SDWF	1.8	16	0.01	0.04	0.03224	0.03224(18)	—
M0	MDWF	1.8	12	0.000678	0.02661	0.02661	0.02539(17)	0.0476(70)
M1	SDWF	1.8	16	0.004	0.03	0.02477, 0.03	0.02477(18)	—
M2	SDWF	1.8	16	0.006	0.03	0.02477	0.02477(18)	—
F1	MDWF	1.8	12	0.002144	0.02144	0.02144	0.02132(17)	−0.0056(80)

Table 2. Domain wall parameters for the light and strange quarks. All quoted values for am_l and am_s are bare quark masses in lattice units. The column DWF corresponds to the chosen domain wall fermion formulation where 'MDWF' corresponds to Möbius domain wall fermions, 'SDWF' to Shamir domain wall fermions. All light quarks are simulated at their unitary value am_l^{uni}. Valence strange quarks were simulated at am_s^{sim}. Note that the value of the physical strange-quark mass am_s^{phys} slightly disagrees with the unitary strange-quark mass am_s^{uni}.

also ensemble F1 and in this way determined the value of the lattice spacing and physical strange-quark mass on this ensemble.

In the valence sector we simulate light, strange and charm-like heavy quarks. The light-quark masses were chosen to be unitary. The strange-quark mass was slightly adjusted (partially quenched) to its physical value as determined in [37], in cases where this was known prior to running the measurements (C1, C2, M1 and M2). Otherwise the unitary value was chosen. The parameters of the light and strange sector are listed in table 2.

Besides the bare quark mass, DWF have two further input parameters that need to be specified in each simulation: the extent of the fifth dimension L_s and the *domain wall height* parameter M_5, respectively (for details see [35, 37]). More specifically, M_5 is the negative mass parameter in the 4-dimensional Wilson Dirac operator which resides in the 5-dimensional DWF Dirac operator. The parameter M_5 can have some effect on both, the rate of exponential decay of the physical modes away from the boundary in the 5th dimension and the energy scale of unphysical modes that are not localised at the boundary. While changing L_s mostly changes the magnitude of residual chiral symmetry breaking, the choice of M_5 in principle changes the ultraviolet properties of the discretisation. Hence, different choices of M_5 lead to in principle different scaling trajectories. The most important consequence is that calculations combining charm quarks with a distinct M_5 from the light quarks must be treated as a mixed action when renormalising flavour off diagonal operators. However, as we will see in section 3.2.2, the difference between treating them as mixed and non-mixed is numerically irrelevant.

Two observations in this context which we made in our quenched DWF studies [34, 35] are crucial for understanding the choice of simulation parameters made here: studying the pseudoscalar heavy-heavy and strange-heavy decay constants we found cut-off effects to be minimal for $M_5 \approx 1.6$. We find that the residual chiral symmetry breaking effects are well suppressed for $L_s = 12$. At the same time we observed a rapid increase in discretisation effects as the bare input quark mass was increased above $am_h \approx 0.4$. Here we work under the assumption that these observations carry over to the case of dynamical simulations with $N_f = 2+1$ flavours which motivates our choice of $M_5 = 1.6$ for charm DWF keeping $am_h \leq 0.4$. As we will see later this assumption is well justified. For the light quarks we use $M_5 = 1.8$ both in the valence- and sea-sector.

All simulated bare charm-quark masses are listed in table 3. Note, that we allow for one exception to the bound $am_h \leq 0.4$ by generating data for $am_h = 0.45$ on ensemble C0. With this we tested whether the reach in the heavy quark mass for DWF with $M_5 = 1.6$ observed in the quenched theory [35] also persists in the dynamical case. The quantity that we monitor in this context is the *residual quark mass* am_{res}, which provides an estimate of residual chiral symmetry breaking in the DWF formalism. It is defined in terms of the axial Ward identity (AWI)

$$a\Delta_\mu^- \langle P(x)\mathcal{A}_\mu(y)\rangle = \langle P(x)\,[2amP(y) + 2J_{5q}(y)]\rangle\,, \tag{2.1}$$

where Δ_μ^- is the lattice backward derivative, am the bare quark mass in lattice units in the Lagrangian, P is the pseudoscalar density and J_{5q} is the pseudoscalar density in the centre of the 5th dimension. It motivates the definition

$$am_{\mathrm{res}} = \frac{\sum\limits_{\mathbf{x}} \langle J_{5q}(x)P(0)\rangle}{\sum\limits_{\mathbf{x}} \langle P(x)P(0)\rangle}\,. \tag{2.2}$$

Figure 1 shows the behaviour of the residual mass on the C0 ensemble. As expected (see reference [35] for details) the residual mass does plateau and remains flat for $am_h \lesssim 0.4$, confirming the validity and upper bound of the mass point at $am_h = 0.4$. The fact that this behaviour is not observed with $am_h = 0.45$ indicates that cut-off effects change in nature when am_h is pushed beyond 0.4, in agreement with our findings in ref. [35]. We therefore exclude any data with $am_h > 0.4$ in the remainder of this paper.

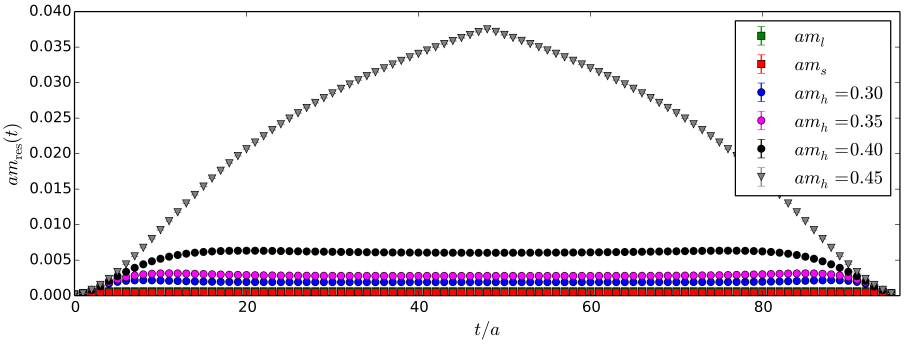

Figure 1. The effective residual mass on the C0 ensemble for all simulated masses.

Name	M_5	L_s	$am_h^{\rm bare}$
C0	1.6	12	0.3, 0.35, 0.4, 0.45
C1	1.6	12	0.3, 0.35, 0.4
C2	1.6	12	0.3, 0.35, 0.4
M0	1.6	8	0.22, 0.28, 0.34, 0.4
M1	1.6	12	0.22, 0.28, 0.34, 0.4
M2	1.6	12	0.22, 0.28, 0.34, 0.4
F1	1.6	12	0.18, 0.23, 0.28, 0.33, 0.4

Table 3. Möbius domain wall parameters for the heavy quarks on all ensembles. All quoted values for am_h are bare quark masses in lattice units. As described in the text, the value indicated in red was only used to verify our assumptions about the applicability of the quenched pilot study to the dynamical case.

3 Data analysis

In this section we describe how we make predictions for the decay constants starting from the evaluation of Euclidean two-point correlation functions on all ensembles and for all parameters discussed above. In particular, from fits to the simulated data we determine pseudoscalar masses m_P and decay constants f_P and ratios thereof, which depend on the simulation parameters (a, m_l, m_h, m_s). Of particular relevance for the analysis are $P = \pi$, K, D, D_s and η_c (the latter one corresponding to an unphysical $c\bar{c}'$ state made of two distinct flavours of quarks having the same charm quark mass). We extrapolate the data for each observable $\mathcal{O}$ to physical light, strange and charm-quark masses as well as to vanishing lattice spacing and infinite volume, $\mathcal{O}(a = 0, m_l^{\rm phys}, m_h^{\rm phys}, m_s^{\rm phys})$.

Besides the decay constants and ratios thereof, for reasons that will become clear later, we will carry out the analysis of the decay constants in terms of the quantity $f_P\sqrt{m_P}$ and only remove the factor $\sqrt{m_P}$ in the final step.

3.1 Correlation functions

In practice we determine the matrix element in equation (1.2) from the time dependence of Euclidean QCD zero-momentum two-point correlation functions,

$$C_{i,MN}(t) \equiv \sum_{\mathbf{x},\mathbf{y}} \langle\, O_{i,M}(t,\mathbf{y})\ (O_{i,N})^{\dagger}\,(0,\mathbf{x})\,\rangle = \sum_{k} \frac{Z_{i,M}^{(k)}\left(Z_{i,N}^{(k)}\right)^{*}}{2E_i^{(k)}} \left(e^{-E_i^{(k)}t} \pm e^{-E_i^{(k)}(T-t)}\right). \tag{3.1}$$

We consider the cases $i = \pi, K, D, D_s$ or η_c. The operators $O_{i,M}$ are interpolating operators with the quantum numbers of the desired mesons, e.g. $O_{D_s,M} = \bar{c}\,\Gamma_M s$, where we consider $\Gamma_A = \gamma_0\gamma_5$ and $\Gamma_P = \gamma_5$, respectively. The sum on the r.h.s. of eq. (3.1) is over excited states k and in practice we will consider the ground and first excited state in the data analysis. The constants $Z_{i,M}^{(k)}$ are defined by $Z_{i,M}^{(k)} = \langle\, P_i^{(k)}\,|\,(O_{i,M})^{\dagger}\,|\,0\,\rangle$ where $P_i^{(k)}$ is the corresponding kth excited meson state.

When computing the quark propagators we use $\mathbb{Z}(2)\times\mathbb{Z}(2)$ stochastic wall sources [48–50] on a large number of time planes. Details of how many different source planes are used for the various ensembles are listed in the column "hits/conf" in table 1. The results on a given gauge configuration are averaged into one bin.

The calculation of the light and strange quark propagators were performed using the HDCG algorithm [51], reducing the numerical cost and hence making this computation feasible. For the heavy quark propagators a CG inverter was used and we monitored satisfactory convergence using the time-slice residual introduced in ref. [52].

Masses and decay constants have been determined by simultaneous multi-channel fits to the two-point correlation functions $C_{i,AP}$ and $C_{i,PP}$ for a given choice of i. We attempted the use of correlated fits, but found the correlation matrix to be too poorly estimated for a reliable inversion. We therefore carry out uncorrelated fits, i.e. assume the correlation matrix to be diagonal (compare ref. [37]).

The statistical precision of the ground state mass and matrix elements is improved by fitting the ground state as well as the first excited state, allowing for earlier time slices (with smaller statistical errors) to contribute to the fit. This was done for $i = D, D_s$, where we are interested in the matrix elements and not merely in the masses as in the case for $i = \pi, \eta_c$. During all these fits the χ^2/d.o.f. were monitored. Tables with the bare results in lattice units on all ensembles can be found in appendix B.

Figure 2 illustrates the correlator fit for the charm-quark mass closest to the physical value on the M0 ensemble. The fit ranges were chosen by systematically varying t_{min} and t_{max}, fixing them in a region where no dependence is observed. Figure 3 shows the ground state results of varying t_{min} and t_{max} for the case of the mass point closest to the physical charm quark mass on the medium ensemble M0.

A first impression of the range of ensembles (lattice spacing, light sea quark mass, charm-quark mass) for which we generated data is given in figure 4, representatively for the ratio of decay constant f_{D_s}/f_D plotted against the inverse of the measured η_c mass.

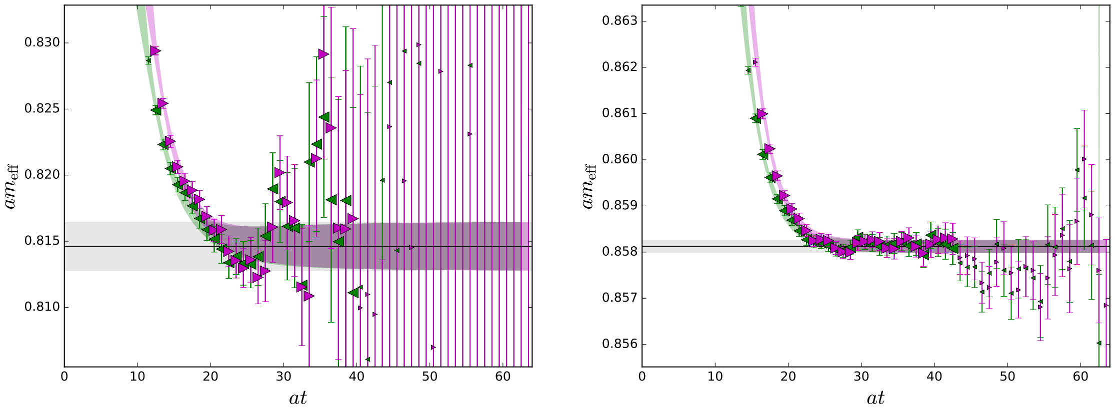

Figure 2. Example of excited state correlation function fits for a heavy-light (left) and heavy-strange (right) meson on the M0 ensemble. The black line and grey shaded region is the fit result for the ground state mass. The green left-facing and magenta right-facing triangles show the effective mass as obtained from the simulated data for $\langle AP\rangle$ and $\langle PP\rangle$, respectively. Larger symbols correspond to data points that enter the fit. The coloured shaded regions are the fit result for the $\langle AP\rangle$ and $\langle PP\rangle$ correlation functions respectively.

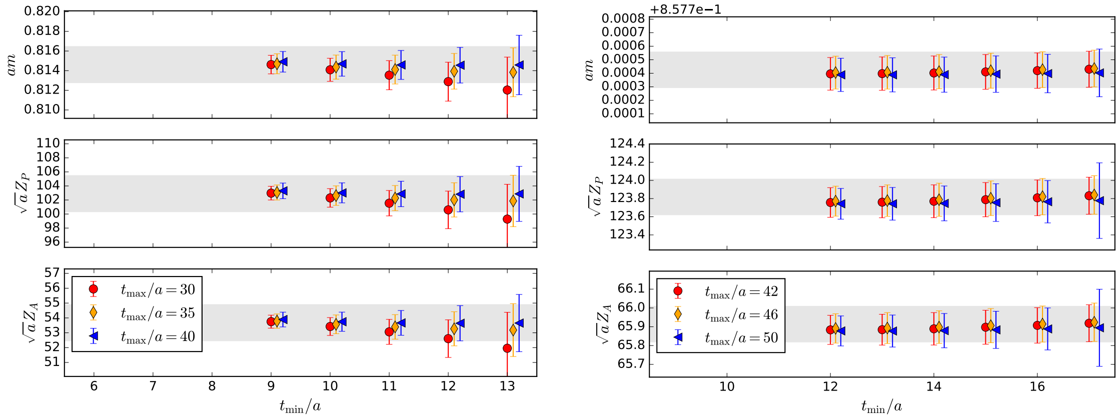

Figure 3. Variation of the time slices included in the correlation function fits for a heavy-light (left) and heavy-strange (right) meson on the M0 ensemble. The grey error band shows the result of the conservatively chosen fit with $t/a \in [12, 41)$ (left) and $t/a \in [15, 44)$ (right).

3.2 Non perturbative renormalisation

To make contact between lattice regulated data and quantities in a continuum theory, the heavy-light current needs to be renormalised. Since we use a mixed action current, by using a different value of M_5 for the light and strange quarks ($M_5 = 1.8$) to the heavy quarks ($M_5 = 1.6$), the usual domain wall axial Ward identity eq. (2.1) is not satisfied.

Since in the free field theory the modification of the action represents a modest change to irrelevant parameters, we might hope the impact on renormalisation constants is small. This is something we can verify. In fact, the estimate of the systematic error arising from this change in action is found to be below percent level, and this is discussed in more detail in section 3.2.2 along with a proposal for the determination of fully non-perturbatively

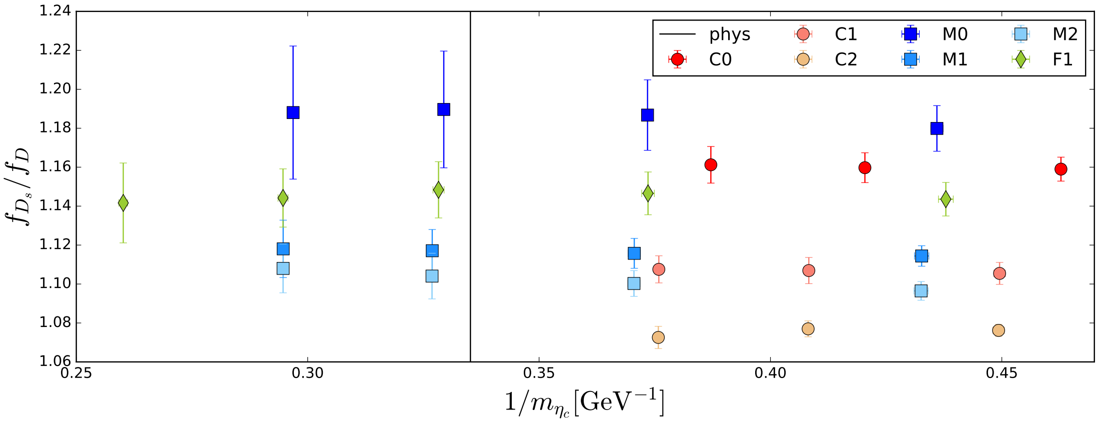

Figure 4. Collected data for the ratio of decay constants f_{D_s}/f_D as obtained from the correlator fits. The solid vertical line labelled “phys” corresponds to the physical η_c mass.

renormalised axial currents using appropriate ratios of off-shell mixed and unmixed action vertex functions.

Since empirically this is indeed a small effect, in all of the following we will extract the renormalisation constants from a light-light unmixed action current and associate a systematic error devised from the non-perturbative renormalisation (NPR) study.

It is worth mentioning that we have recently developed a massive renormalisation scheme [53], RI/mSMOM, by extending the massless RI/SMOM scheme [54, 55], with the renormalised composite fields defined away from the chiral limit. This includes finite masses in one, i.e. the mixed case, or both quark fields entering the bilinear operator. Using this scheme the renormalisation constant for the heavy-light axial current can be extracted non-perturbatively. For more details, refer to ref. [53] and appendix D.

3.2.1 Unmixed action axial current renormalisation constants

The light-light axial renormalisation constant can be found from fitting the time behaviour of the relation

$$Z_A^{\mathrm{eff}}(t) = \frac{1}{2}\left[\frac{C_{\mathcal{A}P}(t-1/2)+C_{\mathcal{A}P}(t+1/2)}{2C_{AP}(t)} + \frac{2C_{\mathcal{A}P}(t+1/2)}{C_{AP}(t-1)+C_{AP}(t+1)}\right] \tag{3.2}$$

to a constant [37, 56]. Here $C_{\mathcal{A}P}(t)$ is the correlation function between the conserved point-split axial vector current defined on the links between the lattice sites [56] and the pseudoscalar density, whilst $C_{AP}(t)$ is the same correlation functions with the conserved axial vector current replaced by the local current one defined on the lattice sites.

The folded time behaviour of the light-light current for all ensembles scaled to the interval $[0, 1)$ is shown in figure 5. As expected we can see a lattice spacing dependence. The slight difference between C1 and C2 (M1 and M2) arises from the slightly different light-quark mass m_l. We can also identify a plateau region to which we can fit a constant to obtain the values of the renormalisation constants. The results of these fits are listed in table 4 and are in good agreement with ref. [37].

JHEP12(2017)008

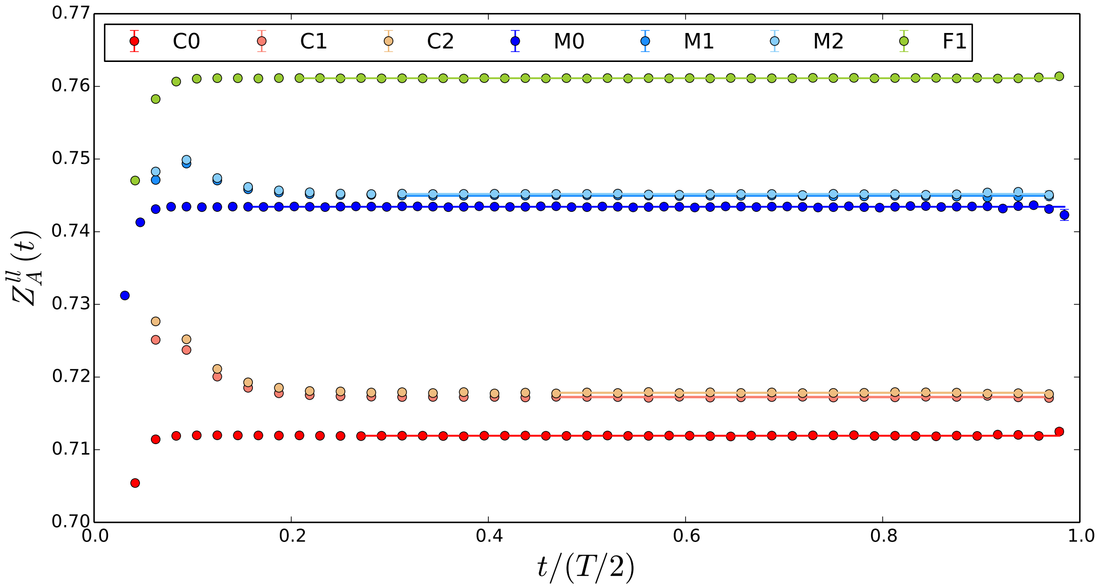

Figure 5. The time behaviour of $Z_A^{\text{eff}}(t)$ scaled to the interval $[0, 1]$ for all ensembles. The solid lines correspond to the fit results obtained by fitting a constant to the plateau region of the data. The fit results are summarised in table 4.

ens	Z_A^{ll}
C0	0.711920(24)
C1	0.717247(67)
C2	0.717831(53)
M0	0.743436(16)
M1	0.744949(39)
M2	0.745190(40)
F1	0.761125(19)

Table 4. The values for Z_A for the various ensembles found from fitting a constant to the time dependence shown in figure 5.

3.2.2 Vertex functions of mixed action current

We use the non-exceptional Rome-Southampton renormalisation scheme, RI/SMOM, [54, 55] to investigate the effects of a change in the action on quantities entering the axial current renormalisation constant. In particular we evaluate the variation of the projected, amputated vertex function for the axial current $\mathcal{P}[\Lambda_{\text{A}}]$, on each of the ensembles C2, M1 and F1.

The details of the numerical computation of the amputated axial vertex function Λ_{A} in the RI/SMOM scheme are discussed in appendix D. Tables 5, 6 and 7 present the ratios of $\mathcal{P}[\Lambda_{\text{A}}]$, for different combinations of actions i.e. $(M_5^1, M_5^2) = (1.8, 1.8), (1.6, 1.8), (1.6, 1.6)$ at around 2 GeV. In all cases the unitary light-quark mass - which is assumed to be sufficiently

JHEP12(2017)008

$(ap)^2$	$p\,[\mathrm{GeV}]$	$\frac{\mathcal{P}[\Lambda_\mathrm{A}](1.8,1.8)}{\mathcal{P}[\Lambda_\mathrm{A}](1.6,1.6)}$	$\frac{\mathcal{P}[\Lambda_\mathrm{A}](1.6,1.8)}{\mathcal{P}[\Lambda_\mathrm{A}](1.6,1.6)}$	$\frac{\mathcal{P}[\Lambda_\mathrm{A}](1.8,1.8)}{\mathcal{P}[\Lambda_\mathrm{A}](1.6,1.8)}$
1.037	1.817	0.996816(35)	0.998149(32)	0.998664(12)
1.133	1.900	0.996878(41)	0.998180(33)	0.998695(14)
1.234	1.982	0.996943(37)	0.998220(29)	0.998721(17)
1.339	2.065	0.997009(31)	0.998263(23)	0.998743(17)
1.448	2.148	0.997084(28)	0.998312(20)	0.998770(15)

Table 5. The ratios of projected amputated vertex function for the axial currents with different actions on the C2 ensemble. The quark mass for both fields is taken to be $am_l = 0.01$.

$(ap)^2$	$p\,[\mathrm{GeV}]$	$\frac{\mathcal{P}[\Lambda_\mathrm{A}](1.8,1.8)}{\mathcal{P}[\Lambda_\mathrm{A}](1.6,1.6)}$	$\frac{\mathcal{P}[\Lambda_\mathrm{A}](1.6,1.8)}{\mathcal{P}[\Lambda_\mathrm{A}](1.6,1.6)}$	$\frac{\mathcal{P}[\Lambda_\mathrm{A}](1.8,1.8)}{\mathcal{P}[\Lambda_\mathrm{A}](1.6,1.8)}$
0.583	1.820	0.996774(55)	0.998139(53)	0.998508(24)
0.637	1.903	0.996805(66)	0.998132(45)	0.998516(32)
0.694	1.985	0.996773(66)	0.998143(34)	0.998520(28)
0.753	2.068	0.996702(88)	0.998143(28)	0.998522(26)
0.814	2.151	0.996658(85)	0.998138(22)	0.998524(22)

Table 6. The ratios of projected amputated vertex function for the axial currents with different actions on the M1 ensemble. The quark mass for both fields is taken to be $am_l = 0.004$.

$(ap)^2$	$p\,[\mathrm{GeV}]$	$\frac{\mathcal{P}[\Lambda_\mathrm{A}](1.8,1.8)}{\mathcal{P}[\Lambda_\mathrm{A}](1.6,1.6)}$	$\frac{\mathcal{P}[\Lambda_\mathrm{A}](1.6,1.8)}{\mathcal{P}[\Lambda_\mathrm{A}](1.6,1.6)}$	$\frac{\mathcal{P}[\Lambda_\mathrm{A}](1.8,1.8)}{\mathcal{P}[\Lambda_\mathrm{A}](1.6,1.8)}$
0.482	1.926	0.996779(23)	0.9982202(85)	0.998555(11)
0.516	1.990	0.996744(26)	0.9982053(99)	0.998539(12)
0.548	2.054	0.996728(24)	0.9981981(91)	0.998525(97)
0.583	2.118	0.996716(19)	0.9981914(85)	0.9985203(79)
0.619	2.183	0.996719(19)	0.998189(10)	0.9985242(64)

Table 7. The ratios of projected amputated vertex function for the axial currents with different actions on the F1 ensemble. The quark mass for both fields is taken to be $am_l = 0.002144$.

close to the chiral limit - is used. The data has been generated using ten gauge field configurations which leads to sufficiently precise results. We see that the ratio $\frac{\mathcal{P}[\Lambda_\mathrm{A}](1.8,1.8)}{\mathcal{P}[\Lambda_\mathrm{A}](1.6,1.6)}$ on each of the ensembles has the largest deviation from unity as compared to the other ratio combinations, which is expected since both the quark fields entering the bilinear have different actions between the numerator and the denominator.

The main feature emerging from this study is that the deviation from unity is at most of order 0.4% across a range of momenta around 2 GeV. This is negligible on the scale of our other uncertainties and for the purposes of the present work we can simply include it as a sub-dominant systematic error.

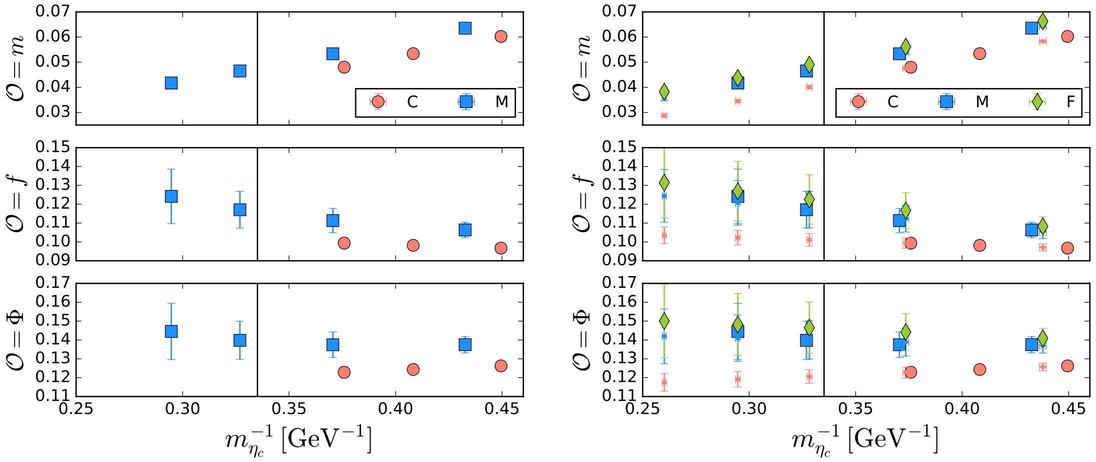

Figure 6. *Left*: values of dimensionless parameters $\alpha_{\mathcal{O}}$ as defined in the text for C1 (red circles) and M1 (blue squares). *Right*: the same data overlaid with an extrapolation to the heavy quark choices of F1 (small red and blue symbols for C1 and M1, respectively). From this, the values of $\alpha_{\mathcal{O}}$ for the fine ensembles F1 (green diamonds) are found, as outlined in the text.

3.3 Strange-quark mass correction

We determine the physical strange-quark mass on all ensembles considered here by repeating the global fit to light meson observables detailed in [37] but including our new fine ensemble F1. At the time of the data generation the values of am_s^{phys} were not yet known for ensembles with near-physical pion masses (C0 and M0) and the new finer ensemble F1. To correct for the resulting small mistuning we repeated the simulation of all charmed meson observables on C1 and M1 with both the unitary and the physical valence strange-quark mass. From this we obtain information on the (small) corrections on C0, M0 and F1. We define the parameters $\alpha_{\mathcal{O}}(a, m_h^i)$ for the different observables $\mathcal{O}$ using

$$\mathcal{O}^{\text{phys}}(a, m_h) = \mathcal{O}^{\text{uni}}(a, m_h)\left(1 + \alpha_{\mathcal{O}}(a, m_h)\,\frac{\Delta m_s}{m_s^{\text{phys}}}\right), \tag{3.3}$$

where $\Delta m_s \equiv m_s^{\text{uni}} - m_s^{\text{phys}}$. The definition of these $\alpha_{\mathcal{O}}(a, m_h^i)$ ensures that they are dimensionless and independent of the renormalisation constants. From the partially quenched data points on C1 and M1 we deduce the values of $\alpha_{\mathcal{O}}(a, m_h^i)$ for $\mathcal{O} = m_{D_s}, f_{D_s}, f\sqrt{m}_{D_s}$ for each choice of the simulated heavy quark mass, as shown in the left panel of figure 6.

To obtain the values for F1, we need to extrapolate $\alpha_{\mathcal{O}}(a, m_h)$ measured on C1 and M1 to (a, m_h) appropriate for F1. Given the linear behaviour in the inverse heavy quark mass evident from the left panel of figure 6, we linearly extrapolate the values for each given lattice spacing to the corresponding $m_h^i(F1)$. This is then extrapolated to the lattice spacing of F1 by fitting the data to

$$\alpha_{\mathcal{O}}(a, m_h^i) = \alpha_{\mathcal{O}}(0, m_h^i) + C_\alpha a^2\,. \tag{3.4}$$

The results for this are shown by the green diamonds in the right-hand panel of figure 6 and summarised in table 8.

spacing	am_h	α_m	α_f	α_Φ
coarse	0.30	0.06026(31)	0.0967(18)	0.1262(20)
	0.35	0.05341(33)	0.0982(22)	0.1243(24)
	0.40	0.04801(37)	0.0994(27)	0.1229(29)
medium	0.22	0.06353(55)	0.1064(41)	0.1375(43)
	0.28	0.05335(70)	0.1113(65)	0.1375(68)
	0.34	0.04650(89)	0.1171(98)	0.140(10)
	0.40	0.0417(11)	0.124(14)	0.145(15)
fine	0.18	0.06630(80)	0.1083(51)	0.1408(53)
	0.23	0.0562(10)	0.1167(94)	0.1442(99)
	0.28	0.0490(12)	0.123(13)	0.147(14)
	0.33	0.0437(14)	0.127(16)	0.148(16)
	0.40	0.0383(16)	0.131(19)	0.150(19)

Table 8. Values of α for the three observables ($\mathcal{O} = m_{D_s}, f_{D_s}, \Phi_{D_s}$). Details about how these were determined can be found in the text.

The maximum extent of the strange-quark mass mistuning is present on M0 and given by $\Delta m_s/m_s^{\mathrm{phys}} = 0.048$. The largest correction (the heaviest charm-quark mass point and the observable $\mathcal{O} = f\sqrt{m_{D_s}}$ on M0) is less than 1%.

3.4 Fixing the physical charm quark

We have a number of possible choices for the meson H that fixes the charm-quark mass. The ones we will consider are $H = D, D_s$ and η_c. Each of these has slightly different advantages and disadvantages attached. The lattice data for the D meson is comparably noisy and has a strong light-quark-mass dependence, making it difficult to disentangle the extrapolation to physical light-quark masses from the interpolation to the physical charm-quark mass. The D_s is statistically cleaner and depends less on the light sea-quark mass than the D, but we need to correct for a mistuning in the valence strange-quark mass as discussed in section 3.3. Finally the η_c is statistically the cleanest, but it differs by quark-disconnected Wick contractions with respect to the corresponding physical particle listed by the Particle Data Group (PDG) [11]. However, this is assumed to be a small effect.[2]

We will investigate all three choices and use the spread as an indication of potential systematic errors. The masses of these mesons, stated by the PDG [11] are

$$\begin{aligned} m_{D^\pm} &= 1.8695(4)\,\mathrm{GeV}, \\ m_{D_s^\pm} &= 1.9690(14)\,\mathrm{GeV}, \\ m_{\eta_c} &= 2.9836(6)\,\mathrm{GeV}. \end{aligned} \tag{3.5}$$

---

[2] Ref. [15] estimates an effect of less than 0.2% for the contributions due to electromagnetic and quark-disconnected distributions to the mass of η_c.

JHEP12(2017)008

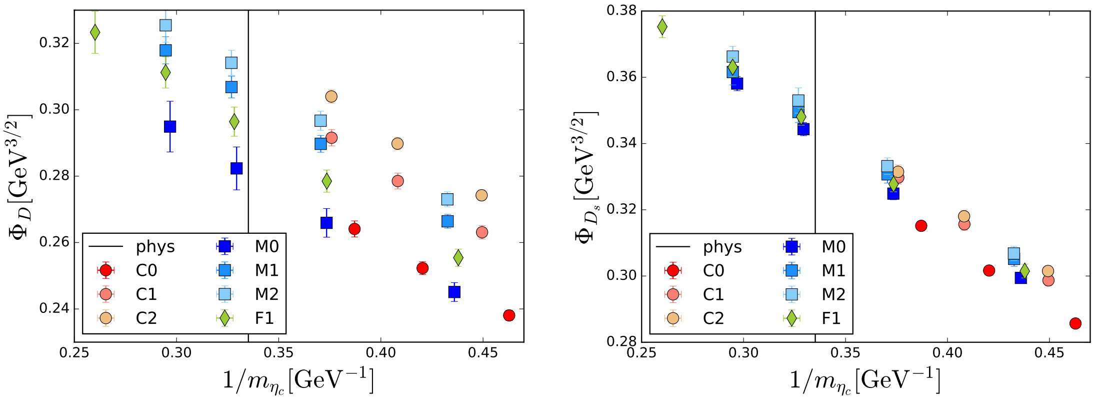

Figure 7. The behaviour of Φ_D (left) and Φ_{D_s} (right) as a function of the inverse η_c mass for the various ensembles. The black vertical line corresponds to the physical value as stated in the PDG [11].

3.5 Global fit

Our fit ansatz corresponds to a Taylor expansion around the physical value of the relevant meson masses. It is given by

$$\begin{aligned}\mathcal{O}(a, m_\pi, m_h) = \mathcal{O}(0, m_\pi^{\rm phys}, m_h^{\rm phys}) \\ + \left[C_{CL}^0 + C_{CL}^1 \, \Delta m_H^{-1}\right] a^2 \\ + \left[C_\chi^0 + C_\chi^1 \, \Delta m_H^{-1}\right] \left(m_\pi^2 - m_\pi^{2\,\rm phys}\right) \\ + \left[C_h^0\right] \Delta m_H^{-1},\end{aligned} \tag{3.6}$$

where $\Delta m_H^{-1} = 1/m_H - 1/m_H^{\rm phys}$ and $H = D, D_s$ or η_c. This means we simultaneously fit the continuum limit dependence (coefficients C_{CL}), the pion mass dependence (coefficients C_χ) and heavy quark dependence (coefficients C_h) as well as cross terms (coefficients linear in $\Delta 1/m_h$, i.e. C_χ^1 and C_{CL}^1) in one global fit. The coefficients C_{CL}^1 and C_χ^1 capture mass dependent continuum limit and pion mass extrapolation terms. This arises by expanding $C_{CL}(m_h)$ and $C_\chi(m_h)$ in powers of Δm_H^{-1}.

Note that following the discussion in section 2, only data with $am_h^{\rm bare} \leq 0.4$ enters the global fits. The global fit therefore includes, on the coarsest ensemble, information only from masses below the physical charm point, but which still contribute to the global fit in both, $O(a^2)$ and mass dependence behaviour, as we extrapolate to the physical charm quark mass in the continuum limit.

When considering the individual decay constants (as opposed to their ratio) we use the quantity $\Phi_{D_{(s)}} = f_{D_{(s)}}\sqrt{m_{D_{(s)}}}$ in the subsequent analysis. As can be seen in figure 7 this quantity is, within statistical resolution, linear in $1/m_{\eta_c}$. Also its dependence on the light (sea and valance) quark-mass, as shown exemplarily in figure 8, is linear irrespective of the heavy-quark mass.

We estimate the systematic uncertainty by limiting the data entering the fit to the case of pion masses not larger than 450, 400 or 350 MeV in turn. Another variation we have already mentioned is the choice of the meson that fixed the charm-quark mass. Finally we

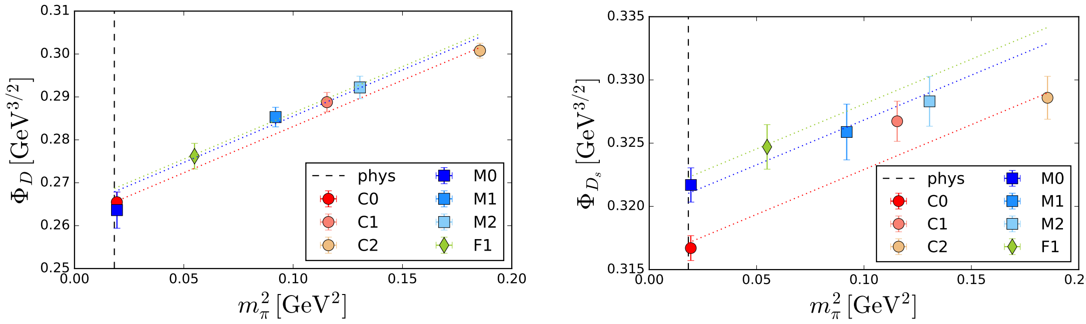

Figure 8. At the current level of statistical resolution the dependence of Φ_D (left) and Φ_{D_s} (right) on the light valence- and sea-quark masses is well described by a linear (in m_π^2) ansatz. The plots representatively show data from all ensembles for the reference point $m_{\eta_c} = 2.61\,\text{GeV}$ to which we interpolated linearly in $1/m_{\eta_c}$. The dashed lines indicate the fitted pion mass dependence for the three lattice spacings.

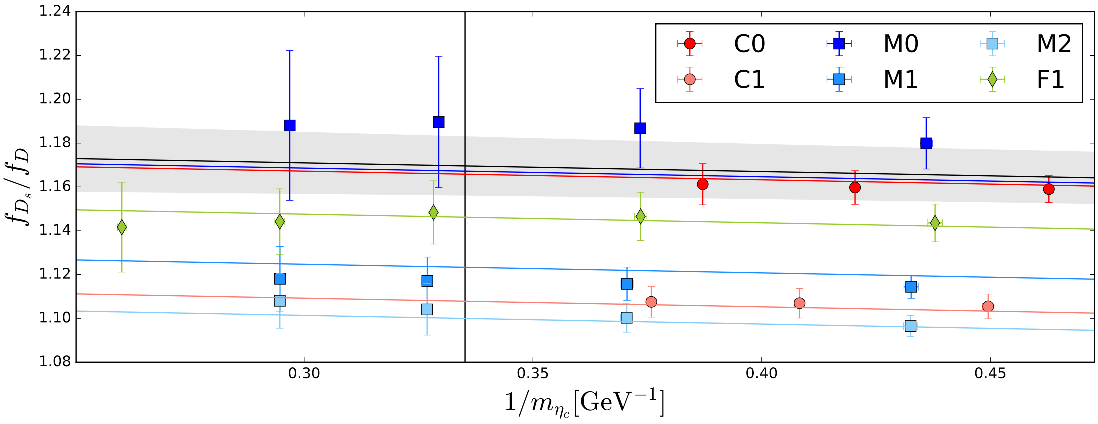

Figure 9. One example for the global fit according to (3.6) for the case of the observable f_{D_s}/f_D. In the case presented here the charm-quark mass is fixed by the η_c meson and a pion mass cut of $m_\pi < 400\text{MeV}$ is employed. The grey band shows the fit result at physical pion masses and vanishing lattice spacing. The coloured bands correspond to the fit projected to the given pion mass and lattice spacing for the corresponding ensembles. In this fit we ignore heavy mass dependent continuum and pion mass terms.

can modify the fit form (3.6) by setting some of the parameters to zero by hand (e.g. C_{CL}^1 and C_χ^1), which we will do when the data is not sufficiently accurate to resolve them clearly.

3.5.1 Global fit for ratio of decay constants

For the ratio of decay constants, fully correlated fits could be achieved. Figure 9 gives one example of such a fully correlated fit for the ratio of decay constants. The fit shown here has a pion mass cut of $m_\pi < 400\text{MeV}$ and uses the η_c mass to fix the charm-quark mass. Furthermore, heavy mass dependent coefficients of the continuum limit and the extrapolation to physical pion masses are ignored (i.e. $C_{CL}^1 = 0$ and $C_\chi^1 = 0$).

Table 14 in appendix C summarises the results of all fit variations for f_{D_s}/f_D. The results of these are also shown in figure 10. The red (blue, green) data points correspond to

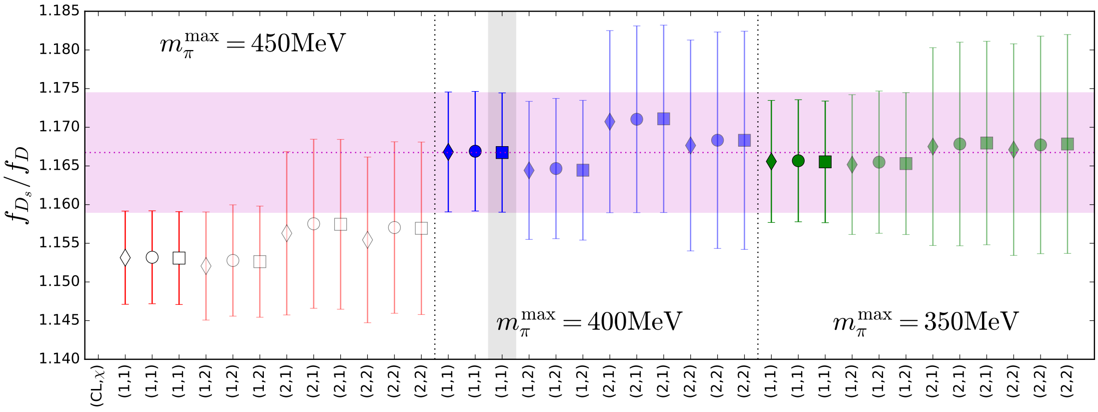

Figure 10. Comparison of the results of the different choices in the global fit. The grey and magenta bands highlight the fit shown in figure 9. The different symbols indicate different ways of fixing the heavy quark mass, i.e. $H = D(\diamond)$, $D_s(\bigcirc)$, and (the connected part of) $\eta_c(\square)$. Fainter data points indicate that at least one of the heavy mass dependent coefficients is compatible with zero at the one sigma level. More detail about the data shown here is given in the text.

pion mass cuts of $m_\pi^{\max} = 450\,\text{MeV}$ ($400\,\text{MeV}$, $350\,\text{MeV}$). The different symbols indicate different ways of fixing the heavy quark mass, i.e. $H = D(\diamond)$, $D_s(\bigcirc)$, and (the connected part of) $\eta_c(\square)$. Finally the label at the x-axis describes which fit was used by stating the number of coefficients for the continuum limit (CL) and pion mass limit (χ) respectively. E.g. fits results labelled $(2,2)$ correspond to the fit form (3.6) whilst $(2,1)$ corresponds to keeping two coefficients for the continuum limit extrapolation, but only one coefficient for the pion mass extrapolation by setting C_χ^1 to zero. Cases where one of the coefficients C_{CL}^1 and C_χ^1 is compatible with zero at the one sigma level are indicated by the corresponding data point being partially transparent.

From the results shown in figure 10 we can make a few observations. We find that the ratio of decay constants is insensitive to the way we fix the charm-quark mass. This is not surprising as the ratio of decay constants does not strongly depend on the heavy quark mass (compare figure 9). We find that a dependence is observed when including pions with $m_\pi > 400\,\text{MeV}$, for this reason we restrict ourselves to $m_\pi \leq 400\,\text{MeV}$. We can also see that when allowing for heavy mass dependent pion mass and continuum extrapolation terms, these can not be resolved with the present data. They also do not significantly change the central value of the fit result but increase the statistical error. This is again not surprising, given the mild behaviour with heavy quark mass displayed by the data.

From this discussion we choose the highlighted fit (i.e. the one presented in figure 9) as our final fit result and as statistical error. We assign the systematic error arising from the fit form from the maximal spread in the central value of the fit results as we vary the parameters of the fit, maintaining $m_\pi \leq 400\,\text{MeV}$. More precisely, we take the maximal difference between the central value of the preferred fit and the central values of all fits with $m_\pi \leq 400\,\text{MeV}$ displayed in figure 10. From this we quote

$$\frac{f_{D_s}}{f_D} = 1.1667(77)(^{+44}_{-23})_{\text{fit}}, \tag{3.7}$$

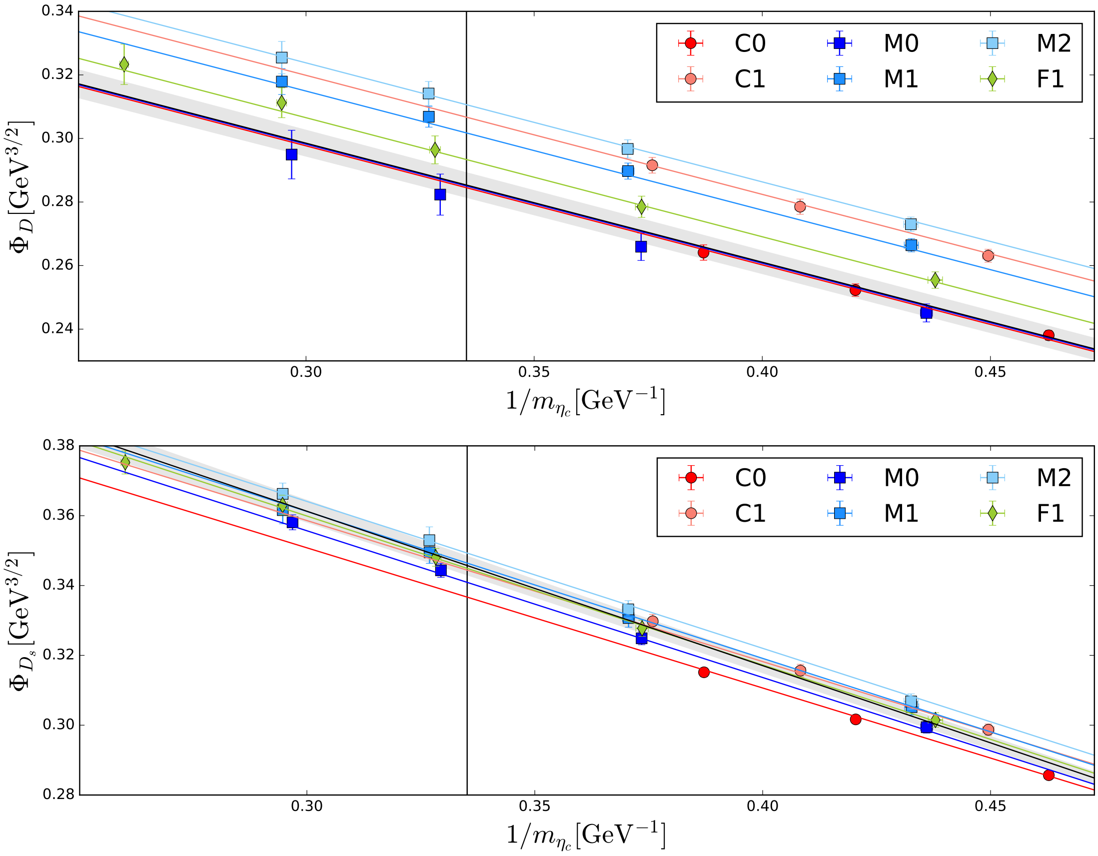

Figure 11. Examples for the global fit according to (3.6) for the case of the observables Φ_D (top) and Φ_{D_s} (bottom). In both cases the charm-quark mass is fixed by the η_c meson and a pion mass cut of $m_\pi < 400\mathrm{MeV}$ is employed. Again, the grey band shows the fit result at physical pion masses and vanishing lattice spacing. The coloured bands correspond to the fit projected to the given pion mass and lattice spacing for the corresponding ensembles. More details about these fits can be found in the text.

where the first error is statistic and the second error captures the systematic error associated with the chiral-continuum limit as well as the way the charm-quark mass is fixed.

3.5.2 Global fit for Φ_D and Φ_{D_s}

Figure 11 shows the chosen fit results for Φ_D (top) and Φ_{D_s} (bottom) respectively. In both cases the heavy quark mass is fixed by the η_c mass and a pion mass cut of $m_\pi \leq 400\,\mathrm{MeV}$ is used. Contrary to the fit of the ratio of decay constants, correlated fits of Φ_D and Φ_{D_s} proved to be unstable. Uncorrelated fits were used instead which lead to slightly larger errors.

Tables 15 and 16 in appendix D summarise the results of all fit variations for Φ_D and Φ_{D_s} respectively. Similar to the previous section we vary the fit parameters to determine the stability of the results. We find that we can consistently resolve the C^1_{CL} coefficient in the case of Φ_{D_s}, whilst this is less clear in the case of Φ_D. For this reason we choose $(CL, \chi) = (1, 1)$ for the case of Φ_D and $(CL, \chi) = (2, 1)$ for the case of Φ_{D_s} (see figure 12).

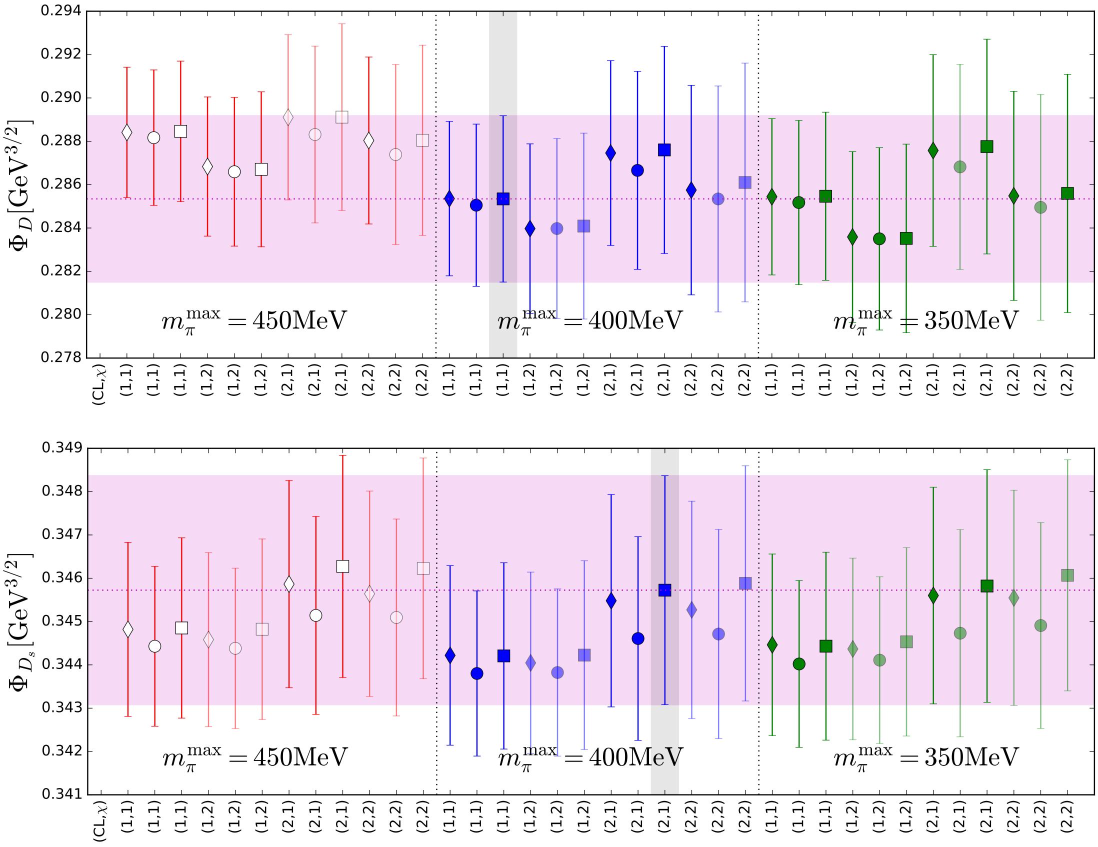

Figure 12. Comparison of the results of the different choices in the global fit for Φ_D (top) and Φ_{D_s} (bottom). The grey and magenta bands highlight the fit shown in figure 11. The different symbols indicate different ways of fixing the heavy quark mass, i.e. $H = D(\Diamond)$, $D_s(\bigcirc)$, and (the connected part of) $\eta_c(\square)$. Fainter data points indicate that at least one of the heavy mass dependent coefficients is compatible with zero at the one sigma level. More detail about the data shown here is given in the text.

Again, little dependence is observed in the case of $m_\pi \leq 400\,\mathrm{MeV}$ so this pion mass cut is used. The dependence is larger in the case of Φ_D than for Φ_{D_s} in agreement with intuition. We see little dependence in the way the heavy quark mass is fixed, even though (contrary to the ratio of decay constants) the heavy mass dependence is now significant. Overall we see more variation in the results of the fit than we have for the ratio of decay constants. Following the same procedure to determine the systematic error associated with the fit as above we find

$$\begin{aligned} \Phi_D &= 0.2853(38)(^{+24}_{-18})_{\mathrm{fit}}\,\mathrm{GeV}^{3/2}, \\ \Phi_{D_s} &= 0.3457(26)(^{+\ 3}_{-19})_{\mathrm{fit}}\,\mathrm{GeV}^{3/2}. \end{aligned} \tag{3.8}$$

To test the robustness of the global fit (3.6) in addition to the pion mass cuts mentioned above, we also investigated the impact of applying mass cuts to the data (i.e. excluding the heaviest and/or lightest data points on each ensemble in a large number of combinations). We find that the central value remains statistically consistent with our final answer in all cases as can be seen in figure 13. It shows that the statistical errors remain essentially

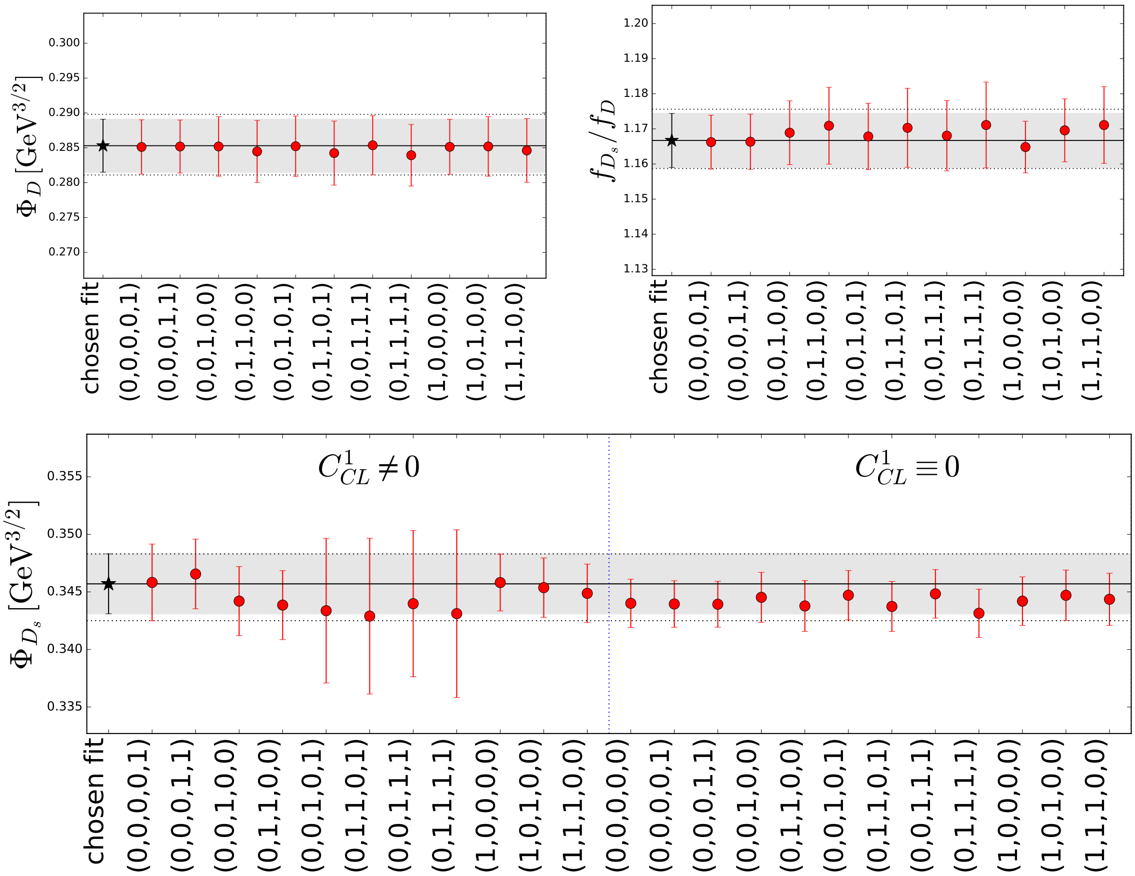

Figure 13. Impact of different heavy mass cuts on the final result of the fit using equation (3.6). The black star shows the chosen fit for Φ_D (top left), f_{D_s}/f_D (top right) and Φ_{D_s} for the preferred fit as discussed above and highlighted by the vertical grey bands in figures 10 and 12. The grey band and grey dotted lines depict the statistical error and total (statistic and systematic error due to the fit as presented in (3.7) and (3.8) added in quadrature), respectively. The red circles show the results of various mass cuts. The set of five numbers label these cuts and correspond in order to the following: (including the $am_h = 0.45$ point on C0; excluding the lightest charm mass point on *all* ensembles; excluding the lightest charm mass point on *all coarse* ensembles; excluding the heaviest charm mass point on *all* ensembles; excluding the heaviest charm mass point on *all coarse* ensembles). In the case of Φ_{D_s} we carry out the fits under these cuts twice: firstly for the choice made above, i.e. allowing for a mass dependence in the continuum limit coefficient ($C^1_{CL} \neq 0$, data left of the blue dotted line) and secondly for the same choice as is made for Φ_D and f_{D_s}/f_D, i.e. fits where C^1_{CL} is set to zero (right of the vertical dotted blue line).

constant for the exclusion of individual data points, but do grow somewhat as a larger number of points (particularly on the same ensembles) are removed.

It should not be surprising that continuing this process to remove several massive data points on the coarsest ensemble, in the case of Φ_{D_s} for which we resolve and use a mass dependent a^2 coefficient, eventually causes a ~2.5 fold increase in the statistical error from our global fit. This is because the mass dependence is removed from the data on the coarsest ensemble and we are left with a poorly constrained fit parameter. If we drop this parameter from the global fit, recognising that the mass is now not varied sufficiently to resolve the mass dependence of the lattice artefacts on this ensemble, the fit quality remains acceptable and there is no increase in the statistical error. The stability of the results under a wide range of cuts (throwing away elements of our data set) substantiates the small quoted systematic errors associated with the global fit and justifies using the selected data points for the final results.

3.6 Systematic error analysis

So far we have discussed central values, statistical errors and the systematic errors due to the fit for the value of Φ_D, Φ_{D_s} and f_{D_s}/f_D and the non-perturbative renormalisation. We now discuss the remaining systematic error budget due to scale setting, mistuning of the strange-quark mass, finite volume and isospin breaking and continuum limit.

The uncertainty in determining the lattice spacing has been propagated throughout the entire analysis by creating a bootstrap distribution with the width of the error quoted in table 1. As a result of this, the correlations between the lattice spacing and dimensionless observables are neglected. The uncertainty in the physical strange-quark masses arising from ref. [37] has been treated in the same way. Both of these are therefore already included in the statistical error.

We have already discussed the systematic error arising from the correction of the mistuning of the strange-quark mass in section 3.3 and came to the conclusion that this yields an uncertainty of $9 \times 10^{-6}\,\mathrm{GeV}^{3/2}$ for Φ_{D_s} and 3×10^{-4} for f_{D_s}/f_D.

We estimate the finite size effects by comparing our values of $m_\pi L$ to a study the MILC collaboration has undertaken [20]. They studied the volume dependence of charmed meson decay constants on ensembles with different volumes whilst keeping the lattice spacings and quark masses constant. This was done for a lattice spacing of 0.12 fm and pion masses of just above 200 MeV. The considered volumes are 2.88 fm, 3.84 fm and 5.76 fm corresponding to values of $m_\pi L$ of 3.2, 4.3 and 5.4, respectively. For the masses of the D and D_s meson they observed variations of $\lesssim 1\,\mathrm{MeV}$ and $\lesssim 0.5\,\mathrm{MeV}$, respectively. For the decay constants the variations they found are $< 0.3\%$ and $< 0.15\%$. Applied to our data, this leads to estimates of the systematic errors of $\delta\Phi_D \approx 0.001\,\mathrm{GeV}^{3/2}$ and $\delta\Phi_{D_s} \approx 0.0006\,\mathrm{GeV}^{3/2}$. We expect f_D and f_{D_s} to be similarly affected by finite size effects, and therefore expect cancellations in the ratio. We conservatively take the larger relative error (0.3%) as an estimate for the ratio, yielding $\delta\frac{f_{D_s}}{f_D} \approx 0.0035$. Given that the minimum value of $m_\pi L$ for our ensembles is 3.8, results derived from these numbers are a good conservative estimate.

In our simulations we treat the up and down quark masses as degenerate, which is not the case in nature, and neglect electromagnetic effects. This affects in particular the masses of the mesons we consider. In principle these effects cannot be disentangled. In the determination of the decay constants we neglect electromagnetic effects since they are defined as pure QCD quantities. However, for the determination of the CKM matrix elements these effects will need to be taken into account [11, 20].

We devise a systematic error associated to the way we fix the heavy quark mass by considering how much the fit result for Φ_D changes when we replace the input mass $m_{D^\pm} = 1.86961(09)\,\mathrm{GeV}$ by $m_{D^0} = 1.86484(05)\,\mathrm{GeV}$ [11]. We estimate the effect of this shift

observable	central	stat	total systematic	fit sys	finite volume	h.o. CL	$m_u \neq m_d$	renormalisation	strange quark
		$\times 10^4$		$\times 10^4$					
Φ_D [GeV$^{3/2}$]	0.2853	38	$^{+29}_{-24}$	$^{+24}_{-18}$	10	—	4.7	11	—
Φ_{D_s} [GeV$^{3/2}$]	0.3457	26	$^{+18}_{-26}$	$^{+\ 3}_{-19}$	6	7	4.4	14	0.9
f_{D_s}/f_D	1.1667	77	$^{+57}_{-43}$	$^{+44}_{-23}$	35	—	8	—	3

Table 9. Summary of the systematic error budget for the quantities Φ_D, Φ_{D_s} and the ratio of decay constants. Details of the discussion leading to these results can be found in the text.

using the fit result of the coefficient C_h^0 for the case of $h = D$ and multiplying these by $\left|m_{D^0}^{-1} - m_{D^\pm}^{-1}\right| \sim 0.0014\,\mathrm{GeV}^{-1}$. From this we find $\delta\Phi_D \sim 0.00037\,\mathrm{GeV}^{3/2}$, $\delta\Phi_{D_s} \sim 0.00044\,\mathrm{GeV}^{3/2}$ and $\delta\frac{f_{D_s}}{f_D} \sim 0.00003$. For the quantity f_{D_s}/f_D this is negligible. As a probe for the same effect in the light-quark mass fixing, we consider the effect of choosing $m_{\pi^\pm}$ instead of m_{π^0} as input mass, i.e. calculating $C_\chi^0\left(m_{\pi^\pm}^2 - m_{\pi^0}^2\right)$. From this we find $\delta\Phi_D \sim 0.00029\,\mathrm{GeV}^{3/2}$, $\delta\Phi_{D_s} \sim 0.00001\,\mathrm{GeV}^{3/2}$ and $\delta\frac{f_{D_s}}{f_D} \sim -0.00080$. Adding these two effects in quadrature we obtain the values listed in the column $m_u \neq m_d$ in table 9.

Given that the continuum limit coefficient C_{CL}^0 is compatible with zero for the fits chosen for Φ_D ($C_{CL}^0 = -0.003(11)\,\mathrm{GeV}^{7/2}$) and $f_{D_s}/f_D = 0.005(25)\,\mathrm{GeV}^2$, we neglect higher order $O(a^4)$ effects. For Φ_{D_s} we find $C_0^{CL} = -0.027(10)\,\mathrm{GeV}^{7/2}$ (the heavy mass dependent continuum limit term vanishes at the physical charm-quark mass). To estimate the impact of higher order discretisation effect terms we write

$$\frac{\delta\Phi_{D_s}}{\Phi_{D_s}} = \frac{1}{\Phi_{D_s}}\left[C_{CL}^0 a^2 + D_{CL}^0 a^4\right] = \frac{C_{CL}^0 a^2}{\Phi_{D_s}}\left[1 + \frac{D_{CL}^0}{C_{CL}^0}a^2\right]. \tag{3.9}$$

Substituting the numbers for C_{CL}^0 and the coarsest and finest lattice spacings we find $C_{CL}^0 a^2/\Phi_{D_s} \sim 0.026$ and 0.010 respectively. Assuming $D_{CL}^0/C_{CL}^0 = (0.5\,\mathrm{GeV})^2$ (i.e. setting the scale such that discretisation effects grow as a/Λ with $\Lambda = 500\,\mathrm{MeV}$) we find $D_{CL}^0/C_{CL}^0 a^2 \sim 0.008$ and ~ 0.003. So the residual discretisation effects are 8% (3%) of the leading discretisation effects, yielding at most 0.2% of the absolute value.

Combining these errors in quadrature we arrive at our final values for $\Phi_{D_{(s)}}$. Using the masses of $D^\pm$ and $D_s^\pm$ [11] (compare eq. (3.5)) we obtain values for the decay constants $f_{D_{(s)}}$,

$$\begin{aligned}
\Phi_D &= 0.2853(38)_{\mathrm{stat}}(^{+29}_{-24})_{\mathrm{sys}}\,\mathrm{GeV}^{3/2} \quad \Rightarrow \quad f_D = 208.7(2.8)_{\mathrm{stat}}(^{+2.1}_{-1.8})_{\mathrm{sys}}\,\mathrm{MeV}\,,\\
\Phi_{D_s} &= 0.3457(26)_{\mathrm{stat}}(^{+18}_{-26})_{\mathrm{sys}}\,\mathrm{GeV}^{3/2} \quad \Rightarrow \quad f_{D_s} = 246.4(1.9)_{\mathrm{stat}}(^{+1.3}_{-1.9})_{\mathrm{sys}}\,\mathrm{MeV}\,.
\end{aligned} \tag{3.10}$$

We are now in a position to compare our results to the results found in the literature. Adding our results to those presented in the most recent FLAG report [21] we obtain the

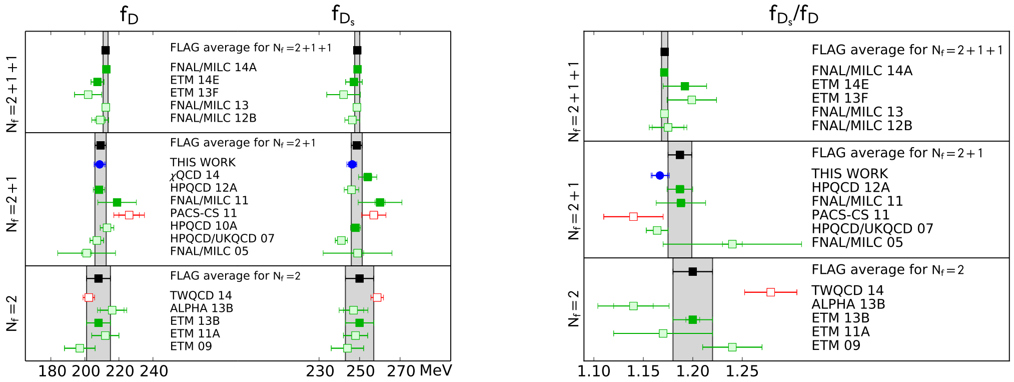

Figure 14. Superposition of our results (blue circles) to the data presented in the most recent FLAG report [21]. The colour scheme of the remaining data points follows the FLAG convention, presented in detail in section 2 of ref [21]. The small error bar shows the statistic error only, whilst the large error band includes both, the statistic and the systematic error.

plots in figure 14. The smaller error bar presents the statistic error only, whilst the larger error bar shows the full error (statistic and systematic). In all cases the error budget is dominated by the statistical error. We find good agreement with the literature and have errors competitive with the other results displayed in figure 14 [15–20, 27, 57–66].

4 CKM matrix elements

Having obtained the decay constants, we can make a prediction of the CKM matrix elements $|V_{cd}|$ and $|V_{cs}|$. However, the values shown in (1.1) are obtained in nature and therefore we need to adjust these values to those of an isospin symmetric theory. In other words, the measured decay rate $|V_{cq}|\, f_{D_q}$ does include electroweak, electromagnetic and isospin breaking effects, so before extracting $|V_{cq}|$ we need to correct the decay rate for these effects. Ref. [20] distinguishes between universal long-distance electromagnetic (EM) effects, universal short distance electroweak (EW) effects and structure dependent EM effects. All of these modify the decay rate to match the experimental value to the theory in which we simulate. The combined effect of the universal long-distance EM and short-distance EW effects is to lower the decay rate by 0.7% [20, 67, 68]. We adjust the decay rates from (1.1) and then calculate the CKM matrix elements from this. We find

$$\begin{aligned} |V_{cd}| &= 0.2185(50)_{\mathrm{exp}}(^{+35}_{-37})_{\mathrm{lat}}, \\ |V_{cs}| &= 1.011(16)_{\mathrm{exp}}(^{+11}_{-\ 9})_{\mathrm{lat}}. \end{aligned} \tag{4.1}$$

Again, we can superimpose our results to those obtained in the most recent FLAG report [21], shown in figure 15. This combines the results of refs. [15–20, 64, 69, 70]. Again we find good agreement between previous works and obtain a competitive error.

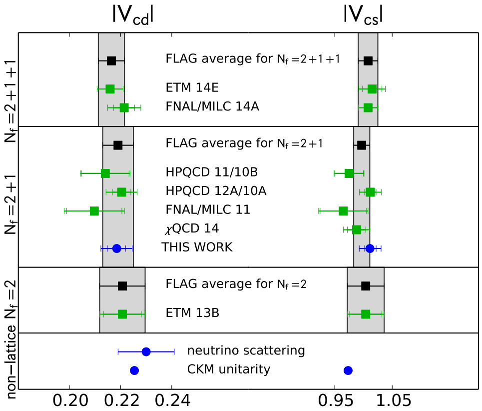

Figure 15. Superposition of our results (blue circles) to the data presented in the most recent FLAG report [21]. The colour scheme of the remaining data points follows the FLAG convention, presented in detail in section 2 of ref [21]. The smaller error bars of our results show the lattice error only, whilst the large error bands include both, the theoretical and the experimental errors, added in quadrature.

5 Conclusion and outlook

In this paper we reported on RBC/UKQCD's first computation of the D- and D_s-meson decay constants on $N_f = 2+1$ domain wall fermion ensembles including physical light quarks and (valence) domain wall charm quarks. The results for decay constants and CKM matrix elements as summarised in the abstract derive from a thorough data analysis by means of a global fit to the data. This fit combines results below and above the physical charm quark mass, two ensembles with physical pion masses and three distinct lattice spacings. With a precision of 1.6% (f_D), 1.0% (f_{D_s}) and 0.7% (f_{D_s}/f_D) the results are competitive and establish domain wall fermions as a powerful discretisation for heavy quarks. We hope that our results will provide useful input to a wide range of applications in (Beyond) Standard Model phenomenology.

Looking ahead, we are exploring changes in the formulation of the domain wall action, such as gauge link smearing, which we found increases the reach in the heavy quark mass on a given ensemble before cut off effects become substantial [71]. This will allow us to do computations directly at the physical charm quark mass also on our coarsest ensemble.

Acknowledgments

We would like to thank our RBC and UKQCD collaborators for their support, in particular to Antonin Portelli for interesting and helpful discussions, to Oliver Witzel for valuable comments and careful reading of the manuscript and to Marina Marinkovic for contributions in the early stages of the charm project.

The research leading to these results has received funding from the European Research Council under the European Union's Seventh Framework Programme (FP7/2007-2013) / ERC Grant agreement 279757 as well as SUPA student prize scheme, Edinburgh Global

$L^3 \times T \times L_s$	$48^3 \times 96 \times 12/a^4$	
β	2.31	
α	2	
steps per HMC traj.	10	
$\delta\tau$	0.1	
Metropolis acceptance	93%	
Plaquette expectation value	0.6279680(23)	$\tau_{\text{int}} = 3.2(5)$
w_0/a	2.3917(25)	$\tau_{\text{int}} = 32(9)$
$\sqrt{t_0}/a$	2.03921(98)	$\tau_{\text{int}} = 27(7)$
am_π	0.08446(18)	
am_K	0.18600(22)	
am_{res} $(am_q = am_l)$	0.0002290(19)	

Table 10. Basic properties of the F1 ensemble.

Research Scholarship and STFC, grants ST/M006530/1, ST/L000458/1, ST/K005790/1, and ST/K005804/1, and the Royal Society, Wolfson Research Merit Awards, grants WM140078 and WM160035. The authors gratefully acknowledge computing time granted through the STFC funded DiRAC facility (grants ST/K005790/1, ST/K005804/1, ST/K000411/1, ST/H008845/1). The software used includes the CPS QCD code (http://qcdoc.phys.columbia.edu/cps.html), supported in part by the USDOE SciDAC program; and the BAGEL (http://www2.ph.ed.ac.uk/∼paboyle/bagel/Bagel.html) assembler kernel generator for high-performance optimised kernels and fermion solvers [72].

A Properties of ensemble F1

Here we present details and properties of ensemble F1 which was generated in order to allow for a continuum limit with three lattice spacings. It has not appeared in any of RBC/UKQCD's previous analyses.

In table 10 we summarise basic simulation parameters and properties for ensemble F1. All integrated autocorrelation times were estimated using the technique described in ref. [73]. We have used the same implementation of the exact hybrid Monte Carlo algorithm for the ensemble generation as in ref. [37], with five intermediate Hasenbusch masses, (0.005,0.017, 0.07 , 0.18, 0.45), for the two-flavor part of the algorithm. A rational approximation was used for the strange quark determinant. See ref. [37] for more details. Figures 16 and 17 show the Monte Carlo evolution and histograms of the topological charge (measured with the GLU package [74]) and the Wilson flow scales w_0 and $\sqrt{t_0}$, respectively. The measured autocorrelation time motivates our choice to separate evaluations of observables on ensemble F1 in the main part of this paper by 40 molecular dynamics steps (for comparison: the separation is 40 on C1 and 20 on all remaining ensembles).

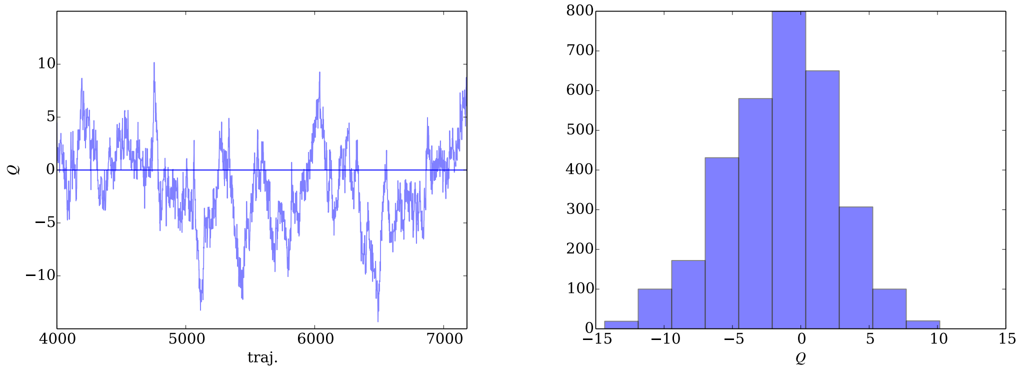

Figure 16. Monte Carlo history and histogram of the topological charge Q. The corresponding estimated integrated autocorrelation time for Q is $\tau_{\text{int}} = 60(2)$ and for Q^2 it is $\tau_{\text{int}} = 34(9)$.

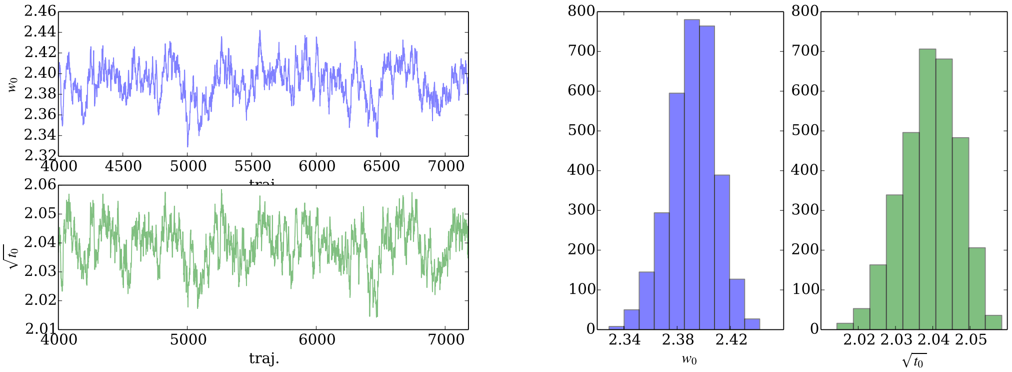

Figure 17. *Left*: Monte Carlo history of Wilson flow scales w_0 and $\sqrt{t_0}$, respectively. *Right*: the corresponding histograms of w_0 and $\sqrt{t_0}$, respectively.

B Correlator fit results

Tables 11, 12 and 13 summarise the fit ranges and the fit results of the correlation function fits to the heavy-light, heavy-strange and heavy-heavy pseudoscalar mesons, respectively. Since the different channels may have a slightly different approach to the ground state (compare figure 2) we quote the smaller value of t_{min}. In all cases $t_{\mathrm{min}}^{AP} \leq t_{\mathrm{min}}^{PP}$. The t_{max} quoted is the first time slice which is *not* included in the fit.

ens	$[t_{\mathrm{min}}, t_{\mathrm{max}})$		am_D	af_D^{bare}	m_D [GeV]	f_D^{ren} [GeV]
C0	8	30	0.82242(82)	0.16211(85)	1.4224(33)	0.1996(11)
	8	30	0.8995(10)	0.1643(11)	1.5558(37)	0.2023(14)
	8	30	0.9727(12)	0.1654(13)	1.6823(41)	0.2036(17)
C1	8	25	0.83111(95)	0.1687(10)	1.4834(44)	0.2160(14)
	8	25	0.9075(11)	0.1710(12)	1.6198(49)	0.2188(16)
	8	22	0.9802(11)	0.1722(12)	1.7495(52)	0.2204(16)
C2	8	25	0.84129(65)	0.17468(62)	1.5015(43)	0.2238(10)
	8	25	0.91722(77)	0.17679(80)	1.6370(47)	0.2265(12)
	8	22	0.98995(85)	0.17851(86)	1.7669(51)	0.2287(13)
M0	11	41	0.63066(95)	0.1146(11)	1.4875(51)	0.2010(21)
	11	41	0.7259(13)	0.1159(17)	1.7122(61)	0.2032(31)
	12	41	0.8146(18)	0.1162(25)	1.9214(72)	0.2037(44)
	12	41	0.8975(22)	0.1156(28)	2.1168(81)	0.2027(50)
M1	9	29	0.63804(77)	0.12168(65)	1.5206(57)	0.2160(14)
	9	27	0.73315(92)	0.12345(80)	1.7473(66)	0.2192(16)
	9	27	0.8211(12)	0.1235(11)	1.9570(75)	0.2193(20)
	9	27	0.9027(14)	0.1221(14)	2.1513(83)	0.2167(25)
M2	9	32	0.64237(80)	0.12424(73)	1.5310(57)	0.2207(15)
	9	32	0.73731(98)	0.12603(97)	1.7572(66)	0.2238(19)
	9	32	0.8252(12)	0.1261(13)	1.9668(76)	0.2240(24)
	9	32	0.9068(16)	0.1247(17)	2.1611(85)	0.2214(32)
F1	11	42	0.53696(70)	0.09913(79)	1.4895(57)	0.2093(18)
	11	41	0.61936(88)	0.1006(10)	1.7181(67)	0.2125(23)
	11	41	0.6960(11)	0.1010(13)	1.9307(77)	0.2133(29)
	11	37	0.7682(12)	0.1010(13)	2.1309(85)	0.2132(29)
	11	37	0.8612(16)	0.0991(18)	2.3889(98)	0.2092(38)

Table 11. Fit results for the masses and decay constants of the D meson on all ensembles. The second set of columns is renormalised where the renormalisation constants are obtained from the light-light conserved current as described in the text.

ens	$[t_{\mathrm{min}}, t_{\mathrm{max}})$		am_{D_s}	$af_{D_s}^{\mathrm{bare}}$	m_{D_s} [GeV]	$f_{D_s}^{\mathrm{ren}}$ [GeV]
C0	12	41	0.88227(13)	0.18809(17)	1.5249(37)	0.23134(64)
	12	41	0.95671(16)	0.19073(22)	1.6536(40)	0.23458(67)
	12	37	1.02773(18)	0.19225(25)	1.7765(42)	0.23645(69)
C1	9	32	0.87662(43)	0.18654(45)	1.5646(49)	0.23880(98)
	9	32	0.95114(46)	0.18923(53)	1.6976(53)	0.2422(11)
	9	32	1.02215(51)	0.19071(62)	1.8243(56)	0.2441(11)
C2	9	32	0.87804(42)	0.18799(43)	1.5671(49)	0.24085(96)
	9	32	0.95235(48)	0.19040(56)	1.6998(52)	0.2439(11)
	9	32	1.02309(56)	0.19146(74)	1.8260(56)	0.2453(12)
M0	14	44	0.678132(88)	0.135920(96)	1.5946(56)	0.23711(92)
	14	44	0.77124(10)	0.13829(13)	1.8144(62)	0.24119(96)
	15	44	0.85813(13)	0.13897(19)	2.0195(68)	0.2423(10)
	15	44	0.93926(16)	0.13817(24)	2.2109(74)	0.2408(11)
M1	13	32	0.67420(41)	0.13560(46)	1.6068(66)	0.2407(13)
	13	32	0.76723(47)	0.13774(64)	1.8285(73)	0.2446(15)
	13	32	0.85376(57)	0.13800(86)	2.0348(81)	0.2450(19)
	13	32	0.93420(71)	0.1365(12)	2.2265(88)	0.2423(23)
M2	12	32	0.67472(41)	0.13623(41)	1.6081(66)	0.2419(13)
	12	32	0.76794(50)	0.13866(56)	1.8302(73)	0.2463(14)
	12	32	0.85470(84)	0.1393(11)	2.0370(83)	0.2473(23)
	12	32	0.93539(64)	0.13812(74)	2.2293(88)	0.2453(17)
F1	14	43	0.57222(21)	0.11343(20)	1.5867(67)	0.2393(12)
	14	43	0.65271(24)	0.11546(26)	1.8100(75)	0.2436(12)
	14	43	0.72795(28)	0.11611(34)	2.0188(82)	0.2450(13)
	14	43	0.79862(33)	0.11562(43)	2.2148(89)	0.2439(15)
	14	43	0.89021(44)	0.11320(61)	2.4689(99)	0.2388(17)

Table 12. Fit results for the masses and decay constants of the D_s meson on all ensembles. The second set of columns is renormalised where the renormalisation constants are obtained from the light-light conserved current as described in the text. The results stated here are those for the strange quark mass closest to the physical one.

ens	$[t_{\mathrm{min}}, t_{\mathrm{max}})$		am_{η_c}	m_{η_c} [GeV]
C0	24	48	1.249409(56)	2.1609(47)
	24	48	1.375320(51)	2.3786(51)
	30	48	1.493579(48)	2.5831(56)
C1	18	32	1.24641(20)	2.2246(62)
	21	32	1.37227(19)	2.4492(68)
	21	32	1.49059(17)	2.6604(74)
C2	20	32	1.24701(20)	2.2257(62)
	24	32	1.37276(18)	2.4501(68)
	24	32	1.49102(16)	2.6612(74)
M0	28	59	0.972488(49)	2.2937(70)
	36	59	1.135329(46)	2.6778(81)
	38	59	1.287084(43)	3.0357(92)
	38	59	1.428269(40)	3.369(10)
M1	22	32	0.96975(18)	2.3112(83)
	23	32	1.13226(15)	2.6985(97)
	23	32	1.28347(13)	3.059(11)
	25	32	1.42374(12)	3.393(12)
M2	22	32	0.97000(19)	2.3118(83)
	24	32	1.13246(18)	2.6990(97)
	24	32	1.28365(16)	3.059(11)
	26	32	1.42384(15)	3.393(12)
F1	31	48	0.82322(10)	2.2836(83)
	31	48	0.965045(93)	2.6770(98)
	31	48	1.098129(86)	3.046(11)
	31	48	1.223360(80)	3.394(12)
	35	48	1.385711(74)	3.844(14)

Table 13. Fit results for the masses of the connected part of the η_c meson on all ensembles.

C Global fit results for f_{D_s}/f_D, Φ_D and Φ_{D_s}

H	$m_\pi^{\rm cut}$	f_{D_s}/f_D	$C_{\rm CL}^0$	$C_{\rm CL}^1$	C_χ^0	C_χ^1	C_h^0	$\chi^2/{\rm dof}$	p
η_c	450	1.1531(60)	0.037(22)	—	−0.529(24)	—	−0.022(16)	0.739	0.803
η_c	450	1.1526(72)	0.036(23)	—	−0.523(59)	−0.03(26)	−0.020(28)	0.773	0.756
η_c	450	1.157(11)	0.019(44)	0.10(21)	−0.527(25)	—	−0.048(56)	0.762	0.769
η_c	450	1.157(11)	0.016(46)	0.11(21)	−0.515(61)	−0.06(26)	−0.045(57)	0.798	0.719
D_s	450	1.1532(60)	0.036(22)	—	−0.529(24)	—	−0.019(14)	0.737	0.806
D_s	450	1.1528(72)	0.036(23)	—	−0.523(58)	−0.02(22)	−0.017(24)	0.771	0.759
D_s	450	1.158(11)	0.018(44)	0.08(17)	−0.527(25)	—	−0.041(47)	0.760	0.772
D_s	450	1.157(11)	0.016(46)	0.09(18)	−0.516(61)	−0.05(22)	−0.038(48)	0.796	0.722
D	450	1.1531(60)	0.036(22)	—	−0.531(25)	—	−0.016(12)	0.740	0.801
D	450	1.1521(70)	0.035(23)	—	−0.516(56)	−0.06(19)	−0.011(20)	0.772	0.758
D	450	1.156(11)	0.023(43)	0.06(15)	−0.530(25)	—	−0.031(40)	0.769	0.762
D	450	1.155(11)	0.019(44)	0.06(15)	−0.510(58)	−0.07(19)	−0.027(41)	0.801	0.716
η_c	400	1.1667(77)	0.005(25)	—	−0.631(44)	—	−0.031(19)	0.319	0.998
η_c	400	1.1644(90)	0.003(25)	—	−0.591(94)	−0.21(43)	−0.019(31)	0.324	0.997
η_c	400	1.171(12)	−0.015(51)	0.11(23)	−0.628(45)	—	−0.056(57)	0.324	0.997
η_c	400	1.168(14)	−0.012(51)	0.08(24)	−0.597(95)	−0.16(44)	−0.041(69)	0.335	0.995
D_s	400	1.1669(77)	0.004(25)	—	−0.631(44)	—	−0.026(16)	0.314	0.998
D_s	400	1.1647(91)	0.003(25)	—	−0.592(94)	−0.17(36)	−0.016(27)	0.319	0.997
D_s	400	1.171(12)	−0.015(50)	0.09(19)	−0.628(45)	—	−0.047(48)	0.320	0.997
D_s	400	1.168(14)	−0.012(51)	0.07(20)	−0.598(94)	−0.13(37)	−0.034(58)	0.332	0.995
D	400	1.1668(78)	0.004(25)	—	−0.634(45)	—	−0.022(14)	0.319	0.998
D	400	1.1644(89)	0.002(25)	—	−0.592(91)	−0.16(31)	−0.013(22)	0.321	0.997
D	400	1.171(12)	−0.014(48)	0.07(16)	−0.631(46)	—	−0.040(42)	0.325	0.997
D	400	1.168(14)	−0.010(49)	0.05(17)	−0.598(92)	−0.13(32)	−0.027(50)	0.335	0.995
η_c	350	1.1655(79)	0.006(26)	—	−0.636(55)	—	−0.025(22)	0.352	0.989
η_c	350	1.1653(92)	0.006(26)	—	−0.63(12)	−0.03(54)	−0.024(32)	0.377	0.982
η_c	350	1.168(13)	−0.005(53)	0.06(25)	−0.635(55)	—	−0.039(65)	0.373	0.982
η_c	350	1.168(14)	−0.005(53)	0.06(25)	−0.63(12)	−0.01(54)	−0.039(70)	0.402	0.970
D_s	350	1.1657(79)	0.005(26)	—	−0.637(55)	—	−0.022(18)	0.349	0.990
D_s	350	1.1655(92)	0.005(26)	—	−0.63(12)	−0.02(45)	−0.021(28)	0.374	0.982
D_s	350	1.168(13)	−0.004(53)	0.04(21)	−0.635(55)	—	−0.032(55)	0.371	0.983
D_s	350	1.168(14)	−0.004(53)	0.04(21)	−0.63(12)	−0.01(45)	−0.032(59)	0.400	0.971
D	350	1.1656(79)	0.005(26)	—	−0.639(56)	—	−0.018(16)	0.352	0.989
D	350	1.1652(90)	0.005(26)	—	−0.63(12)	−0.04(39)	−0.017(23)	0.377	0.982
D	350	1.168(13)	−0.003(52)	0.03(18)	−0.638(56)	—	−0.027(47)	0.375	0.982
D	350	1.167(14)	−0.003(52)	0.03(18)	−0.63(12)	−0.03(39)	−0.025(50)	0.403	0.970

Table 14. Fit results of the different versions of the global fit ansatz (3.6) for the observable f_{D_s}/f_D.

H	m_π^{cut}	$\Phi_D[\mathrm{GeV}^{3/2}]$	C^0_{CL}	C^1_{CL}	C^0_χ	C^1_χ	C^0_h	χ^2/dof
η_c	450	0.2885(32)	−0.010(10)	—	0.203(13)	—	−0.3797(86)	0.555
η_c	450	0.2867(36)	−0.012(10)	—	0.234(26)	−0.36(21)	−0.354(18)	0.459
η_c	450	0.2891(43)	−0.014(17)	0.05(11)	0.204(13)	—	−0.390(30)	0.577
η_c	450	0.2880(44)	−0.021(17)	0.11(12)	0.237(26)	−0.39(21)	−0.374(31)	0.460
D_s	450	0.2882(31)	−0.018(10)	—	0.200(12)	—	−0.3061(70)	0.540
D_s	450	0.2866(34)	−0.020(10)	—	0.228(23)	−0.29(16)	−0.285(15)	0.447
D_s	450	0.2883(41)	−0.019(16)	0.009(91)	0.201(12)	—	−0.308(24)	0.565
D_s	450	0.2874(42)	−0.025(16)	0.056(94)	0.230(24)	−0.31(17)	−0.296(25)	0.460
D	450	0.2884(30)	−0.0202(95)	—	0.176(11)	—	−0.2717(59)	0.578
D	450	0.2868(32)	−0.0228(96)	—	0.205(21)	−0.30(13)	−0.251(12)	0.446
D	450	0.2891(38)	−0.024(14)	0.043(77)	0.177(12)	—	−0.281(20)	0.598
D	450	0.2880(39)	−0.030(15)	0.081(80)	0.209(22)	−0.32(14)	−0.267(21)	0.443
η_c	400	0.2853(38)	−0.003(11)	—	0.230(22)	—	−0.3747(97)	0.300
η_c	400	0.2841(43)	−0.005(11)	—	0.255(40)	−0.32(33)	−0.356(22)	0.255
η_c	400	0.2876(48)	−0.017(18)	0.17(13)	0.233(23)	—	−0.409(32)	0.269
η_c	400	0.2861(55)	−0.015(19)	0.14(14)	0.254(40)	−0.28(34)	−0.386(44)	0.237
D_s	400	0.2851(37)	−0.011(11)	—	0.227(22)	—	−0.3016(79)	0.279
D_s	400	0.2840(42)	−0.012(11)	—	0.248(37)	−0.25(26)	−0.288(17)	0.241
D_s	400	0.2867(46)	−0.021(17)	0.11(10)	0.230(22)	—	−0.323(25)	0.265
D_s	400	0.2853(52)	−0.020(18)	0.08(11)	0.248(37)	−0.22(27)	−0.306(35)	0.237
D	400	0.2854(36)	−0.014(11)	—	0.203(20)	—	−0.2670(66)	0.316
D	400	0.2840(39)	−0.015(11)	—	0.230(34)	−0.30(22)	−0.250(14)	0.232
D	400	0.2875(43)	−0.026(16)	0.135(87)	0.207(21)	—	−0.294(22)	0.271
D	400	0.2857(48)	−0.025(16)	0.103(92)	0.229(34)	−0.26(22)	−0.273(29)	0.209
η_c	350	0.2855(39)	−0.005(12)	—	0.235(25)	—	−0.372(11)	0.348
η_c	350	0.2835(43)	−0.006(12)	—	0.281(48)	−0.56(40)	−0.346(22)	0.238
η_c	350	0.2878(50)	−0.018(19)	0.17(14)	0.239(25)	—	−0.407(35)	0.312
η_c	350	0.2856(55)	−0.017(19)	0.14(14)	0.281(48)	−0.53(40)	−0.378(43)	0.209
D_s	350	0.2852(38)	−0.013(11)	—	0.232(24)	—	−0.2996(87)	0.319
D_s	350	0.2835(42)	−0.014(11)	—	0.272(45)	−0.43(31)	−0.280(17)	0.225
D_s	350	0.2868(47)	−0.022(18)	0.11(11)	0.235(25)	—	−0.322(28)	0.304
D_s	350	0.2850(52)	−0.022(18)	0.09(11)	0.272(45)	−0.41(32)	−0.299(34)	0.214
D	350	0.2854(36)	−0.015(11)	—	0.208(23)	—	−0.2639(73)	0.352
D	350	0.2836(39)	−0.017(11)	—	0.252(40)	−0.45(25)	−0.244(14)	0.209
D	350	0.2876(44)	−0.028(17)	0.134(93)	0.213(23)	—	−0.292(24)	0.300
D	350	0.2855(48)	−0.028(17)	0.111(93)	0.253(40)	−0.42(26)	−0.268(28)	0.169

Table 15. Fit results of the different versions of the global fit ansatz (3.6) for the observable Φ_D.

H	m_π^{cut}	$\Phi_{D_s}[\text{GeV}^{3/2}]$	C^0_{CL}	C^1_{CL}	C^0_χ	C^1_χ	C^0_h	χ^2/dof
η_c	450	0.3449(21)	−0.0206(68)	—	0.0655(92)	—	−0.4167(38)	0.297
η_c	450	0.3448(21)	−0.0206(69)	—	0.066(16)	−0.01(14)	−0.4162(76)	0.311
η_c	450	0.3463(26)	−0.0286(98)	0.114(65)	0.0665(92)	—	−0.440(15)	0.262
η_c	450	0.3462(25)	−0.0287(100)	0.115(66)	0.068(16)	−0.02(14)	−0.440(16)	0.274
D_s	450	0.3444(18)	−0.0294(59)	—	0.0622(80)	—	−0.3345(30)	0.261
D_s	450	0.3444(19)	−0.0294(60)	—	0.064(14)	−0.02(10)	−0.3337(56)	0.273
D_s	450	0.3451(23)	−0.0334(87)	0.051(50)	0.0628(80)	—	−0.345(12)	0.258
D_s	450	0.3451(23)	−0.0336(88)	0.052(50)	0.065(14)	−0.02(10)	−0.344(12)	0.270
D	450	0.3448(20)	−0.0327(66)	—	0.0364(88)	—	−0.2952(27)	0.359
D	450	0.3446(20)	−0.0331(67)	—	0.044(13)	−0.086(91)	−0.2914(50)	0.349
D	450	0.3459(24)	−0.0388(91)	0.073(45)	0.0378(88)	—	−0.311(11)	0.336
D	450	0.3456(24)	−0.0394(92)	0.074(45)	0.045(13)	−0.089(91)	−0.307(10)	0.323
η_c	400	0.3442(22)	−0.0185(68)	—	0.073(14)	—	−0.4175(40)	0.278
η_c	400	0.3442(22)	−0.0185(69)	—	0.073(21)	0.01(18)	−0.4179(77)	0.293
η_c	400	0.3457(26)	−0.027(10)	0.122(70)	0.075(14)	—	−0.442(16)	0.235
η_c	400	0.3459(27)	−0.028(10)	0.127(71)	0.072(21)	0.05(18)	−0.445(18)	0.246
D_s	400	0.3438(19)	−0.0275(59)	—	0.070(12)	—	−0.3348(32)	0.243
D_s	400	0.3438(19)	−0.0274(60)	—	0.069(19)	0.01(13)	−0.3353(57)	0.256
D_s	400	0.3446(24)	−0.0322(90)	0.058(53)	0.071(12)	—	−0.347(12)	0.236
D_s	400	0.3447(24)	−0.0324(90)	0.062(54)	0.069(19)	0.03(13)	−0.348(14)	0.248
D	400	0.3442(21)	−0.0310(66)	—	0.044(13)	—	−0.2951(28)	0.358
D	400	0.3440(21)	−0.0314(66)	—	0.050(19)	−0.08(12)	−0.2920(51)	0.359
D	400	0.3455(25)	−0.0386(93)	0.087(48)	0.046(13)	—	−0.313(11)	0.318
D	400	0.3453(25)	−0.0382(92)	0.080(47)	0.049(19)	−0.05(12)	−0.309(12)	0.328
η_c	350	0.3444(22)	−0.0202(69)	—	0.079(15)	—	−0.4152(42)	0.268
η_c	350	0.3445(22)	−0.0201(69)	—	0.075(26)	0.06(23)	−0.4167(72)	0.284
η_c	350	0.3458(27)	−0.028(10)	0.113(72)	0.080(15)	—	−0.438(17)	0.224
η_c	350	0.3461(27)	−0.029(10)	0.119(68)	0.073(26)	0.09(22)	−0.442(16)	0.232
D_s	350	0.3440(19)	−0.0290(60)	—	0.075(13)	—	−0.3331(34)	0.227
D_s	350	0.3441(19)	−0.0290(60)	—	0.072(22)	0.04(17)	−0.3344(54)	0.240
D_s	350	0.3447(24)	−0.0332(91)	0.052(54)	0.076(13)	—	−0.344(13)	0.223
D_s	350	0.3449(24)	−0.0334(90)	0.056(52)	0.071(22)	0.06(16)	−0.346(12)	0.234
D	350	0.3445(21)	−0.0330(67)	—	0.049(14)	—	−0.2924(30)	0.326
D	350	0.3444(21)	−0.0331(67)	—	0.053(22)	−0.05(15)	−0.2911(48)	0.346
D	350	0.3456(25)	−0.0398(94)	0.079(49)	0.051(14)	—	−0.309(12)	0.288
D	350	0.3455(25)	−0.0397(93)	0.077(46)	0.052(22)	−0.02(15)	−0.308(11)	0.309

Table 16. Fit results of the different versions of the global fit ansatz (3.6) for the observable Φ_{D_s}.

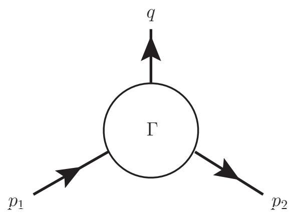

Figure 18. Kinematics used for the correlators of fermion bilinears. Here we have $\Gamma = \mathrm{A} = \gamma^\mu\gamma^5$.

D RI/SMOM and the axial vertex function

The projected axial vertex functions are generated according to the SMOM renormalisation condition [55]:

$$\lim_{\overline{m}\to 0} \frac{1}{12q^2} \mathrm{Tr}\left[\left(q\cdot\Lambda_{\mathrm{A},R}\right)\gamma_5 \not{q}\right]\Big|_{\mathrm{sym}} = 1, \tag{D.1}$$

where $\Lambda_{\mathrm{A},R}$ is the amputated axial vertex function and the subscript R denotes a renormalised quantity. The momentum q out of the vertex satisfies the symmetric non-exceptional condition:

$$p_1^2 = p_2^2 = q^2. \tag{D.2}$$

The momenta are determined by

$$ap_\mu = n_\mu \frac{2\pi}{L_\mu/a}\,, \tag{D.3}$$

for every lattice spacing L such that the magnitude of p is around 2 GeV for an integer n. Note that in order to reach the intermediate momenta we use twisting [75]:

$$ap_\mu = \left(n_\mu + \frac{\theta_\mu}{2}\right)\frac{2\pi}{L_\mu/a}\,. \tag{D.4}$$

Eq. (D.1) can be written in terms of the amputated bare vertex function, the field renormalisation Z_q and the axial operator renormalisation Z_A as follows,

$$\lim_{\overline{m}\to 0} \frac{1}{12q^2}\frac{Z_{\mathrm{A}}}{Z_q} \mathrm{Tr}\left[\left(q\cdot\Lambda_{\mathrm{A}}\right)\gamma_5 \not{q}\right]\Big|_{\mathrm{sym}} = 1, \tag{D.5}$$

where the bare quantity is what is computed numerically on the lattice. Above we have denoted

$$\mathcal{P}[\Lambda_A] \equiv \lim_{\overline{m}\to 0} \frac{1}{12q^2} \mathrm{Tr}\left[\left(q\cdot\Lambda_{\mathrm{A}}\right)\gamma_5 \not{q}\right]\Big|_{\mathrm{sym}}. \tag{D.6}$$

In principle, if the action is substantially changed for the heavy as compared to light quarks, it is possible in the massless renormalisation scheme, to apply the axial RI-SMOM condition (D.1) to the mixed action bilinear

$$\mathcal{P}[\Lambda_{\mathrm{A}}](1.6, 1.8) = \frac{\sqrt{Z_q^1}\sqrt{Z_q^2}}{Z_A^{12}}. \tag{D.7}$$

Again, the indices $i = 1, 2$ refer to the action of the first and second quark field entering the bilinear operator. In the chiral limit, it is possible to systematically eliminate the factors of the quark field renormalisation Z_q from the SMOM condition [53]. However, since we can compute the corresponding unmixed vertex functions, and know how to determine Z_A^{11} and Z_A^{22} from the conserved domain wall current as in eq. (3.2), we are able to determine the axial current renormalisation, Z_A^{12}, from ratios of vertex functions as follows:

$$\frac{(\mathcal{P}[\Lambda_{\mathrm{A}}](1.6, 1.6))\,(\mathcal{P}[\Lambda_{\mathrm{A}}](1.8, 1.8))}{(\mathcal{P}[\Lambda_{\mathrm{A}}](1.6, 1.8))^2} = \frac{\left(Z_A^{12}\right)^2}{Z_A^{11} Z_A^{22}}. \tag{D.8}$$

This result is an interesting, and fully non-perturbative, analogue of the Fermilab [76] partially-perturbative approach to currents that are conserved in the continuum. The ratio of vertex functions in our case is very near unity since the difference in the actions of the quark legs is very small, as is seen in tables 5, 6 and 7.

Furthermore, if the RI-SMOM conditions are modified we can form a consistent set of conditions in the massive case [53]. Since the axial current is partially conserved in the continuum, the difference between the schemes is necessarily only a lattice artefact, implying that either approach may be taken when we take the continuum limit, and yields a universal result. The scaling violations will of course differ between these approaches and for the present paper we have taken the simpler approach of using the near massless vertex function data to define the scaling trajectory for axial current matrix elements.

References

- [1] CLEO collaboration, M. Artuso et al., *Improved measurement of $B(D^+ \to \mu^+\nu)$ and the pseudoscalar decay constant $f(D^+)$*, Phys. Rev. Lett. **95** (2005) 251801 [`hep-ex/0508057`] [INSPIRE].
- [2] CLEO collaboration, M. Artuso et al., *Measurement of the decay constant $f(D_S^+)$ using $D_S^+ \to \ell^+\nu$*, Phys. Rev. Lett. **99** (2007) 071802 [`arXiv:0704.0629`] [INSPIRE].
- [3] CLEO collaboration, B.I. Eisenstein et al., *Precision measurement of $B(D^+ \to \mu^+\nu)$ and the pseudoscalar decay constant $f(D^+)$*, Phys. Rev. **D 78** (2008) 052003 [`arXiv:0806.2112`] [INSPIRE].
- [4] CLEO collaboration, J.P. Alexander et al., *Measurement of $BD_s^+ \to \ell^+\nu$ and the decay constant $f(D_s^+)$ from $600\,pb^{-1}$ of $e^\pm$ annihilation data near $4170\,MeV$*, Phys. Rev. **D 79** (2009) 052001 [`arXiv:0901.1216`] [INSPIRE].
- [5] CLEO collaboration, P. Naik et al., *Measurement of the pseudoscalar decay constant $f(D_s)$ using $D_s^+ \to \tau^+\nu$, $\tau^+ \to \rho^+\bar{\nu}$ decays*, Phys. Rev. **D 80** (2009) 112004 [`arXiv:0910.3602`] [INSPIRE].
- [6] CLEO collaboration, K.M. Ecklund et al., *Measurement of the absolute branching fraction of $D_s^+ \to \tau^+\nu_\tau$ decay*, Phys. Rev. Lett. **100** (2008) 161801 [`arXiv:0712.1175`] [INSPIRE].

[7] CLEO collaboration, P.U.E. Onyisi et al., *Improved measurement of absolute branching fraction of $D_s^+ \to \tau^+\nu_\tau$*, Phys. Rev. **D 79** (2009) 052002 [arXiv:0901.1147] [INSPIRE].

[8] BESIII collaboration, M. Ablikim et al., *Precision measurements of $B(D^+ \to \mu^+\nu_\mu)$, the pseudoscalar decay constant $f(D^+)$ and the quark mixing matrix element $|V_{\rm cd}|$*, Phys. Rev. **D 89** (2014) 051104 [arXiv:1312.0374] [INSPIRE].

[9] Belle collaboration, A. Zupanc et al., *Measurements of branching fractions of leptonic and hadronic D_s^+ meson decays and extraction of the D_s^+ meson decay constant*, JHEP **09** (2013) 139 [arXiv:1307.6240] [INSPIRE].

[10] BaBar collaboration, P. del Amo Sanchez et al., *Measurement of the absolute branching fractions for $D_s^- \to \ell^-\bar{\nu}_\ell$ and extraction of the decay constant $f(D_s)$*, Phys. Rev. **D 82** (2010) 091103 [arXiv:1008.4080] [INSPIRE].

[11] Particle Data Group collaboration, C. Patrignani et al., *Review of particle physics*, Chin. Phys. **C 40** (2016) 100001 [INSPIRE].

[12] S. Aoki et al., *Review of lattice results concerning low-energy particle physics*, Eur. Phys. J. **C 74** (2014) 2890 [arXiv:1310.8555] [INSPIRE].

[13] J. Charles et al., *Current status of the standard model CKM fit and constraints on $\Delta F = 2$ new physics*, Phys. Rev. **D 91** (2015) 073007 [arXiv:1501.05013] [INSPIRE].

[14] M. Bona et al., *Unitarity Triangle analysis in the standard model from UTfit*, talk given at *2016 International Conference on High Energy Physics (ICHEP 2016)*, August 3–10, Chicago, U.S.A. (2016).

[15] C.T.H. Davies, C. McNeile, E. Follana, G.P. Lepage, H. Na and J. Shigemitsu, *Update: Precision D_s decay constant from full lattice QCD using very fine lattices*, Phys. Rev. **D 82** (2010) 114504 [arXiv:1008.4018] [INSPIRE].

[16] Fermilab Lattice, MILC collaborations, A. Bazavov et al., *B- and D-meson decay constants from three-flavor lattice QCD*, Phys. Rev. **D 85** (2012) 114506 [arXiv:1112.3051] [INSPIRE].

[17] H. Na, C.T.H. Davies, E. Follana, G.P. Lepage and J. Shigemitsu, *$|V_{cd}|$ from D meson leptonic decays*, Phys. Rev. **D 86** (2012) 054510 [arXiv:1206.4936] [INSPIRE].

[18] Y.-B. Yang et al., *Charm and strange quark masses and f_{D_s} from overlap fermions*, Phys. Rev. **D 92** (2015) 034517 [arXiv:1410.3343] [INSPIRE].

[19] N. Carrasco et al., *Leptonic decay constants f_K, f_D, and $f(D_s)$ with $N_f = 2+1+1$ twisted-mass lattice QCD*, Phys. Rev. **D 91** (2015) 054507 [arXiv:1411.7908] [INSPIRE].

[20] Fermilab Lattice, MILC collaborations, A. Bazavov et al., *Charmed and light pseudoscalar meson decay constants from four-flavor lattice QCD with physical light quarks*, Phys. Rev. **D 90** (2014) 074509 [arXiv:1407.3772] [INSPIRE].

[21] S. Aoki et al., *Review of lattice results concerning low-energy particle physics*, Eur. Phys. J. **C 77** (2017) 112 [arXiv:1607.00299] [INSPIRE].

[22] HPQCD/UKQCD collaboration, E. Follana et al., *Highly improved staggered quarks on the lattice, with applications to charm physics*, Phys. Rev. **D 75** (2007) 054502 [hep-lat/0610092] [INSPIRE].

[23] A.X. El-Khadra, A.S. Kronfeld and P.B. Mackenzie, *Massive fermions in lattice gauge theory*, Phys. Rev. **D 55** (1997) 3933 [hep-lat/9604004] [INSPIRE].

[24] H. Neuberger, *Exactly massless quarks on the lattice*, *Phys. Lett.* **B 417** (1998) 141 [hep-lat/9707022] [INSPIRE].

[25] K. Osterwalder and E. Seiler, *Gauge field theories on the lattice*, *Annals Phys.* **110** (1978) 440 [INSPIRE].

[26] ALPHA collaboration, A. Juttner and J. Rolf, *A precise determination of the decay constant of the D_s meson in quenched QCD*, *Phys. Lett.* **B 560** (2003) 59 [hep-lat/0302016] [INSPIRE].

[27] J. Heitger, G.M. von Hippel, S. Schaefer and F. Virotta, *Charm quark mass and D-meson decay constants from two-flavour lattice QCD*, PoS(LATTICE 2013)475 [arXiv:1312.7693] [INSPIRE].

[28] S.L. Glashow, J. Iliopoulos and L. Maiani, *Weak interactions with lepton-hadron symmetry*, *Phys. Rev.* **D 2** (1970) 1285 [INSPIRE].

[29] RBC/UKQCD collaboration, N. Christ et al., *Calculating the $K_L - K_S$ mass difference and ϵ_K to sub-percent accuracy*, PoS(LATTICE2013)397 [arXiv:1402.2577] [INSPIRE].

[30] Z. Bai, N.H. Christ, T. Izubuchi, C.T. Sachrajda, A. Soni and J. Yu, *K_L-K_S mass difference from lattice QCD*, *Phys. Rev. Lett.* **113** (2014) 112003 [arXiv:1406.0916] [INSPIRE].

[31] RBC/UKQCD collaboration, N.H. Christ et al., *Prospects for a lattice computation of rare kaon decay amplitudes: $K \to \pi\ell^+\ell^-$ decays*, *Phys. Rev.* **D 92** (2015) 094512 [arXiv:1507.03094] [INSPIRE].

[32] N.H. Christ, X. Feng, A. Juttner, A. Lawson, A. Portelli and C.T. Sachrajda, *First exploratory calculation of the long-distance contributions to the rare kaon decays $K \to \pi\ell^+\ell^-$*, *Phys. Rev.* **D 94** (2016) 114516 [arXiv:1608.07585] [INSPIRE].

[33] RBC/UKQCD collaboration, N.H. Christ et al., *Prospects for a lattice computation of rare kaon decay amplitudes II $K \to \pi\nu\bar{\nu}$ decays*, *Phys. Rev.* **D 93** (2016) 114517 [arXiv:1605.04442] [INSPIRE].

[34] Y.-G. Cho et al., *Improved lattice fermion action for heavy quarks*, *JHEP* **05** (2015) 072 [arXiv:1504.01630] [INSPIRE].

[35] P. Boyle et al., *An exploratory study of heavy domain wall fermions on the lattice*, *JHEP* **04** (2016) 037 [arXiv:1602.04118] [INSPIRE].

[36] N. Carrasco et al., *QED corrections to hadronic processes in lattice qcd*, *Phys. Rev.* **D 91** (2015) 074506 [arXiv:1502.00257] [INSPIRE].

[37] RBC/UKQCD collaboration, T. Blum et al., *Domain wall QCD with physical quark masses*, *Phys. Rev.* **D 93** (2016) 074505 [arXiv:1411.7017] [INSPIRE].

[38] RBC/UKQCD collaboration, C. Allton et al., *Physical results from $2+1$ flavor domain wall QCD and* SU(2) *chiral perturbation theory*, *Phys. Rev.* **D 78** (2008) 114509 [arXiv:0804.0473] [INSPIRE].

[39] Y. Aoki et al., *Continuum limit of B_K from $2+1$ flavor domain wall QCD*, *Phys. Rev.* **D 84** (2011) 014503 [arXiv:1012.4178] [INSPIRE].

[40] RBC/UKQCD collaboration, Y. Aoki et al., *Continuum limit physics from $2+1$ flavor domain wall QCD*, *Phys. Rev.* **D 83** (2011) 074508 [arXiv:1011.0892] [INSPIRE].

[41] Y. Iwasaki and T. Yoshie, *Renormalization group improved action for* SU(3) *lattice gauge theory and the string tension*, *Phys. Lett.* **143B** (1984) 449 [INSPIRE].

[42] Y. Iwasaki, *Renormalization group analysis of lattice theories and improved lattice action: two-dimensional nonlinear $O(N)$ σ-model*, *Nucl. Phys.* **B 258** (1985) 141 [inSPIRE].

[43] R.C. Brower, H. Neff and K. Orginos, *Mobius fermions: improved domain wall chiral fermions*, *Nucl. Phys. Proc. Suppl.* **140** (2005) 686 [`hep-lat/0409118`] [inSPIRE].

[44] R.C. Brower, H. Neff and K. Orginos, *Mobius fermions*, *Nucl. Phys. Proc. Suppl.* **153** (2006) 191 [`hep-lat/0511031`] [inSPIRE].

[45] R.C. Brower, H. Neff and K. Orginos, *The Möbius domain wall fermion algorithm*, *Comput. Phys. Commun.* **220** (2017) 1 [`arXiv:1206.5214`] [inSPIRE].

[46] D.B. Kaplan, *A method for simulating chiral fermions on the lattice*, *Phys. Lett.* **B 288** (1992) 342 [`hep-lat/9206013`] [inSPIRE].

[47] Y. Shamir, *Chiral fermions from lattice boundaries*, *Nucl. Phys.* **B 406** (1993) 90 [`hep-lat/9303005`] [inSPIRE].

[48] UKQCD collaboration, M. Foster and C. Michael, *Quark mass dependence of hadron masses from lattice QCD*, *Phys. Rev.* **D 59** (1999) 074503 [`hep-lat/9810021`] [inSPIRE].

[49] UKQCD collaboration, C. McNeile and C. Michael, *Decay width of light quark hybrid meson from the lattice*, *Phys. Rev.* **D 73** (2006) 074506 [`hep-lat/0603007`] [inSPIRE].

[50] P.A. Boyle, A. Juttner, C. Kelly and R.D. Kenway, *Use of stochastic sources for the lattice determination of light quark physics*, *JHEP* **08** (2008) 086 [`arXiv:0804.1501`] [inSPIRE].

[51] P.A. Boyle, *Hierarchically deflated conjugate gradient*, `arXiv:1402.2585` [inSPIRE].

[52] A. Juttner and M. Della Morte, *Heavy quark propagators with improved precision using domain decomposition*, `PoS(LAT2005)204` [`hep-lat/0508023`] [inSPIRE].

[53] P. Boyle, L. Del Debbio and A. Khamseh, *Massive momentum-subtraction scheme*, *Phys. Rev.* **D 95** (2017) 054505 [`arXiv:1611.06908`] [inSPIRE].

[54] G. Martinelli, C. Pittori, C.T. Sachrajda, M. Testa and A. Vladikas, *A general method for nonperturbative renormalization of lattice operators*, *Nucl. Phys.* **B 445** (1995) 81 [`hep-lat/9411010`] [inSPIRE].

[55] C. Sturm, Y. Aoki, N.H. Christ, T. Izubuchi, C.T.C. Sachrajda and A. Soni, *Renormalization of quark bilinear operators in a momentum-subtraction scheme with a nonexceptional subtraction point*, *Phys. Rev.* **D 80** (2009) 014501 [`arXiv:0901.2599`] [inSPIRE].

[56] P.A. Boyle, *Conserved currents for mobius domain wall fermions*, `PoS(LATTICE2014)087` [`arXiv:1411.5728`] [inSPIRE].

[57] P. Dimopoulos et al., *Pseudoscalar decay constants f_K/f_π, f_D and f_{D_s} with $N_f = 2+1+1$ ETMC configurations*, `PoS(LATTICE2013)314` [`arXiv:1311.3080`] [inSPIRE].

[58] Fermilab Lattice, MILC collaborations, A. Bazavov et al., *Charmed and strange pseudoscalar meson decay constants from HISQ simulations*, `PoS(LATTICE 2013)405` [`arXiv:1312.0149`] [inSPIRE].

[59] Fermilab Lattice, MILC collaborations, A. Bazavov et al., *Pseudoscalar meson physics with four dynamical quarks*, `PoS(LATTICE 2012)159` [`arXiv:1210.8431`] [inSPIRE].

[60] PACS-CS collaboration, Y. Namekawa et al., *Charm quark system at the physical point of 2 + 1 flavor lattice QCD*, *Phys. Rev.* **D 84** (2011) 074505 [`arXiv:1104.4600`] [inSPIRE].

[61] HPQCD/UKQCD collaboration, E. Follana et al., *High precision determination of the π, K, D and D_s decay constants from lattice QCD*, *Phys. Rev. Lett.* **100** (2008) 062002 [`arXiv:0706.1726`] [INSPIRE].

[62] C. Aubin et al., *Charmed meson decay constants in three-flavor lattice QCD*, *Phys. Rev. Lett.* **95** (2005) 122002 [`hep-lat/0506030`] [INSPIRE].

[63] TWQCD collaboration, W.-P. Chen et al., *Decay Constants of Pseudoscalar D-mesons in Lattice QCD with Domain-Wall Fermion*, *Phys. Lett.* **B 736** (2014) 231 [`arXiv:1404.3648`] [INSPIRE].

[64] ETM collaboration, N. Carrasco et al., *B-physics from $N_f = 2$ tmQCD: the standard model and beyond*, *JHEP* **03** (2014) 016 [`arXiv:1308.1851`] [INSPIRE].

[65] ETM collaboration, P. Dimopoulos et al., *Lattice QCD determination of m_b, f_B and f_{B_s} with twisted mass Wilson fermions*, *JHEP* **01** (2012) 046 [`arXiv:1107.1441`] [INSPIRE].

[66] ETM collaboration, B. Blossier et al., *Pseudoscalar decay constants of kaon and D-mesons from $N_f = 2$ twisted mass Lattice QCD*, *JHEP* **07** (2009) 043 [`arXiv:0904.0954`] [INSPIRE].

[67] T. Kinoshita, *Radiative corrections to π-e decay*, *Phys. Rev. Lett.* **2** (1959) 477 [INSPIRE].

[68] A. Sirlin, *Large $m(W)$, $m(Z)$ behavior of the $O(\alpha)$ corrections to semileptonic processes mediated by W*, *Nucl. Phys.* **B 196** (1982) 83 [INSPIRE].

[69] H. Na, C.T.H. Davies, E. Follana, G.P. Lepage and J. Shigemitsu, *The $D \to K, l\nu$ semileptonic decay scalar form factor and $|V_{cs}|$ from lattice QCD*, *Phys. Rev.* **D 82** (2010) 114506 [`arXiv:1008.4562`] [INSPIRE].

[70] H. Na et al., *$D \to \pi, l\nu$ semileptonic decays, $|V_{cd}|$ and 2^{nd} row unitarity from lattice QCD*, *Phys. Rev.* **D 84** (2011) 114505 [`arXiv:1109.1501`] [INSPIRE].

[71] P. Boyle et al., *Charm physics with domain wall fermions and physical pion masses*, `arXiv:1611.06804` [INSPIRE].

[72] P.A. Boyle, *The BAGEL assembler generation library*, *Comput. Phys. Commun.* **180** (2009) 2739 [INSPIRE].

[73] ALPHA collaboration, U. Wolff, *Monte Carlo errors with less errors*, *Comput. Phys. Commun.* **156** (2004) 143 [*Erratum ibid.* **176** (2007) 383] [`hep-lat/0306017`] [INSPIRE].

[74] R. Hudspith, https://github.com/RJhudspith/GLU.

[75] RBC/UKQCD collaboration, R. Arthur and P.A. Boyle, *Step scaling with off-shell renormalisation*, *Phys. Rev.* **D 83** (2011) 114511 [`arXiv:1006.0422`] [INSPIRE].

[76] S. Hashimoto et al., *Lattice QCD calculation of $\bar{B} \to D$ lepton anti-neutrino decay form-factors at zero recoil*, *Phys. Rev.* **D 61** (1999) 014502 [`hep-ph/9906376`] [INSPIRE].